
An Open-Source Framework for Coupled Vehicle-Bridge Interaction Analysis Using OpenSees

Mohammad Talebi-Kalaleh

Department of Civil and Environmental Engineering
University of Alberta, Edmonton, Canada

Qipei Mei*

Department of Civil and Environmental Engineering
University of Alberta, Edmonton, Canada

Abstract

Vehicle-bridge interaction (VBI) is important for simulating bridge response under moving vehicular loads and supports applications such as dynamic amplification studies, weigh-in-motion, and indirect bridge monitoring. Although VBI theory is well established, many existing implementations use custom finite element code or research-specific solvers, which limits their reuse. This paper presents an open-source Python framework for VBI analysis built on OpenSees. The bridge and vehicle are modeled as separate OpenSees subsystems and connected through an iterative scheme that exchanges displacement and force values at each time step until convergence. Five vehicle model types are supported, from a single-axle spring-mass system to two-axle composite half-cars with body pitch and separate tyre and suspension elements. A decoupled mode is also provided: the vehicle static weight is applied as a moving load on the bridge, and the resulting bridge motion is then used as base excitation for the vehicle. Validation against three published benchmarks (quarter-car, half-car with pitch, and full composite models) shows close agreement, with R^2 above 0.998 in all cases. A parametric study reports the accuracy of the decoupled mode as a function of vehicle-to-bridge mass ratio, span length, speed, road roughness class, and background traffic density, and indicates when the decoupled mode is adequate and when full coupling is needed. The complete framework and benchmark configurations are released as open-source software to support reproducible research in vehicle-bridge dynamics.

Keywords vehicle-bridge interaction · OpenSees · iterative partitioned coupling · moving mass · moving load · indirect bridge monitoring · open-source software

1 Introduction

The dynamic interaction between moving vehicles and bridge structures is a classical problem in structural engineering that has attracted sustained research attention for more than half a century [1,2]. When a vehicle traverses a bridge, the coupled dynamics of the two subsystems produce responses that differ, sometimes substantially, from those predicted by simpler models that treat the vehicle as a static or moving force. The vehicle-bridge interaction (VBI) problem supports a range of engineering applications, including: (i) evaluating the dynamic amplification of bridge responses for design and assessment, (ii) bridge weigh-in-motion systems that infer vehicle axle loads from bridge response measurements, and (iii) extracting bridge condition information from the dynamic response of instrumented vehicles passing over the bridge, commonly referred to as indirect or drive-by bridge monitoring [3,4].

The theoretical treatment of VBI dates back to the early works of Fryba [1], who provided analytical solutions for beams subjected to moving forces and moving masses. Yang, Yau, and Wu [2] later developed a comprehensive VBI element formulation in which the vehicle degrees of freedom are condensed into the bridge element matrices at the contact points, enabling a monolithic solution of the coupled system. This formulation was extended to asymmetric two-axle (half-car) vehicles with body pitch by Yang et al. [5], and has served as a primary reference for validating VBI implementations. Parallel efforts by Green and Cebon

*Corresponding author: qipei.mei@ualberta.ca

[6], Zhu and Law [7], and others established iterative partitioned coupling as an alternative to the monolithic approach. In the partitioned scheme, the bridge and vehicle are solved as independent subsystems with interaction forces and displacements exchanged iteratively at each time step until convergence is achieved. This approach offers greater flexibility, as the subsystems can use different solvers, meshes, and integration parameters.

These applications span the full spectrum of VBI use, from forward simulation for design and dynamic amplification studies to inverse analysis for weigh-in-motion and condition assessment. In particular, the growth of drive-by monitoring has recently expanded research interest in VBI simulation. Yang et al. [3] first demonstrated that bridge natural frequencies appear in the spectrum of a passing vehicle’s acceleration response, laying the theoretical foundation for drive-by bridge inspection. Subsequent work by OBrien and colleagues [8,9,10], Malekjafarian et al. [4,11], Eshkevari et al. [12], and Mei et al. [13,14] has advanced the field considerably, developing methods for frequency extraction, damping identification, mode shape estimation, and damage detection from drive-by measurements. All of these applications depend critically on the fidelity of the VBI model used for their development and validation. The present work targets general VBI analysis rather than any single application, providing a reusable simulation platform that can serve design, weigh-in-motion, and monitoring studies alike.

Despite the maturity of VBI theory, its implementation remains a barrier for many researchers and engineers. Most existing implementations are coded from scratch using custom finite element routines or analytical modal superposition, requiring substantial expertise in computational mechanics. Purpose-built VBI codes are typically maintained within individual research groups and are rarely shared as reusable, well-documented software. Meanwhile, established general-purpose finite element packages such as OpenSees [15], which are widely used in the structural engineering community, do not natively support moving load or moving mass analysis.

This paper addresses this gap by presenting an open-source Python framework that performs VBI analysis using OpenSees as the underlying finite element engine. The key idea is to model the bridge and vehicle as separate OpenSees finite element models, each defined using standard OpenSees elements (beam-column elements for the bridge, zero-length spring-dashpot elements for the vehicle), and to couple them externally through a Python-level iterative algorithm. This approach requires no modification to the OpenSees source code and no custom element formulations. At each time step, the framework constructs the vehicle input (bridge deformation plus road roughness at the axle locations), solves the vehicle model for one step to obtain updated reaction forces, maps these forces back onto bridge nodes, solves the bridge model, and iterates until the bridge response converges. The framework supports four vehicle model types of increasing complexity, multi-span bridge configurations, ISO 8608 road roughness generation, and both fully coupled (iterative) and decoupled (moving load) analysis modes.

The remainder of this paper is organised as follows. Section 2 reviews the theoretical background and existing methods for VBI analysis. Section 3 describes the proposed framework in detail, including the bridge and vehicle finite element formulations, the iterative coupling algorithm, the road roughness model, and the simplified decoupled approach. Section 4 validates the framework against established benchmark configurations from the literature. Section 5 presents a parametric study comparing the coupled and decoupled approaches across a range of problem parameters. Section 6 discusses the main observations, implications, and limitations. Section 7 summarises the findings and outlines directions for future development.

2 Literature Review

2.1 Analytical Foundations

The simplest dynamic loading model treats the vehicle as a constant force moving at speed v , for which Fryba [1] derived closed-form solutions using modal superposition. Because this model ignores the vehicle’s inertia, it cannot capture the feedback between the vehicle’s vibration and the bridge’s deformation, which is the defining feature of the vehicle-bridge interaction (VBI) problem.

In the VBI formulation, two physical mechanisms act simultaneously. First, the vehicle undergoes base excitation: each axle follows the bridge surface, whose vertical profile equals the sum of the structural deflection $w(x, t)$ and the road surface roughness $r(x)$. The resulting contact-point displacement

$$u_c(t) = u(x_a(t), t) + r(x_a(t)) \quad (1)$$

where $x_a(t)$ is the axle position, drives the vehicle's equations of motion from below. Second, the bridge experiences the vehicle as a moving dynamic load: the spring, dashpot, and inertial forces that the vehicle transmits at each contact point act as time-varying forces on the beam. Because the bridge deflection depends on the vehicle forces, which in turn depend on the bridge deflection, the two subsystems must be solved together at each time step. Figure 1 illustrates this coupled problem for a two-axle vehicle traversing a simply supported beam.

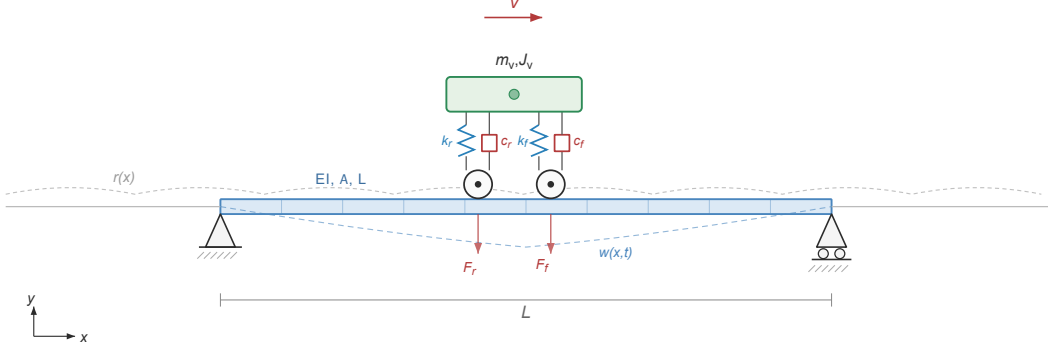


Figure 1: Schematic of the vehicle-bridge interaction problem. A multi-DOF vehicle traverses an Euler-Bernoulli beam bridge at velocity v , with interaction forces F_r and F_f transmitted at the rear and front axle positions through shape function interpolation.

2.2 Vehicle Models

The framework supports four vehicle model types of increasing complexity, illustrated in Figure 2. All models are driven by the contact-point displacement u_c defined in Equation 1, and all transmit a contact force back to the bridge that equals the reaction at the constrained axle node. The governing equations for each model are given below; gravity loads produce a static component that is computed once at the start of the analysis and omitted from the dynamic equations that follow.

The single-axle simple model (Figure 2 a) represents the vehicle as a lumped mass m connected to the contact point through a spring k and dashpot c . With the mass displacement denoted y , the equation of motion is

$$m \ddot{y} + c \dot{y} + k y = c \dot{u}_c + k u_c \quad (2)$$

and the contact force transmitted to the bridge is $F_c = k(y - u_c) + c(\dot{y} - \dot{u}_c)$. Yang and Yau [2] used this model to derive analytical VBI solutions and to validate finite element formulations.

The quarter-car model (Figure 2 b) separates the vehicle into a sprung mass m_s (body) and an unsprung mass m_u (axle/wheel assembly), connected through a suspension (k_s, c_s). The axle is connected to the contact point through a tyre (k_t, c_t). This two-degree-of-freedom model captures both the low-frequency body bounce and the higher-frequency axle hop, making it the standard model for drive-by bridge monitoring studies [9,12]. The equations of motion are

$$\begin{bmatrix} m_u & 0 \\ 0 & m_s \end{bmatrix} \begin{Bmatrix} \ddot{y}_u \\ \ddot{y}_s \end{Bmatrix} + \begin{bmatrix} c_t + c_s & -c_s \\ -c_s & c_s \end{bmatrix} \begin{Bmatrix} \dot{y}_u \\ \dot{y}_s \end{Bmatrix} + \begin{bmatrix} k_t + k_s & -k_s \\ -k_s & k_s \end{bmatrix} \begin{Bmatrix} y_u \\ y_s \end{Bmatrix} = \begin{Bmatrix} c_t \dot{u}_c + k_t u_c \\ 0 \end{Bmatrix} \quad (3)$$

where y_u and y_s are the axle and body displacements. Only the tyre layer connects to the bridge, so the contact force is $F_c = k_t(y_u - u_c) + c_t(\dot{y}_u - \dot{u}_c)$.

The half-car model with pitch (Figure 2 c) extends the formulation to two-axle vehicles. The body, with mass m_v and pitch moment of inertia J_v , undergoes vertical translation y_v and rotation θ_v about its centre of gravity (CG). The rear and front suspensions (k_r, c_r and k_f, c_f) connect the body directly to the two contact points, without separate axle masses. Defining d_1 as the distance from the CG to the front axle and d_2 as the distance from the CG to the rear axle (Figure 2 c), and denoting the rear and front contact-point displacements by u_{cr} and u_{cf} , the bounce equation is

$$m_v \ddot{y}_v + (c_r + c_f) \dot{y}_v + (k_r + k_f) y_v + (d_1 c_f - d_2 c_r) \dot{\theta}_v + (d_1 k_f - d_2 k_r) \theta_v = k_r u_{cr} + k_f u_{cf} + c_r \dot{u}_{cr} + c_f \dot{u}_{cf} \quad (4)$$

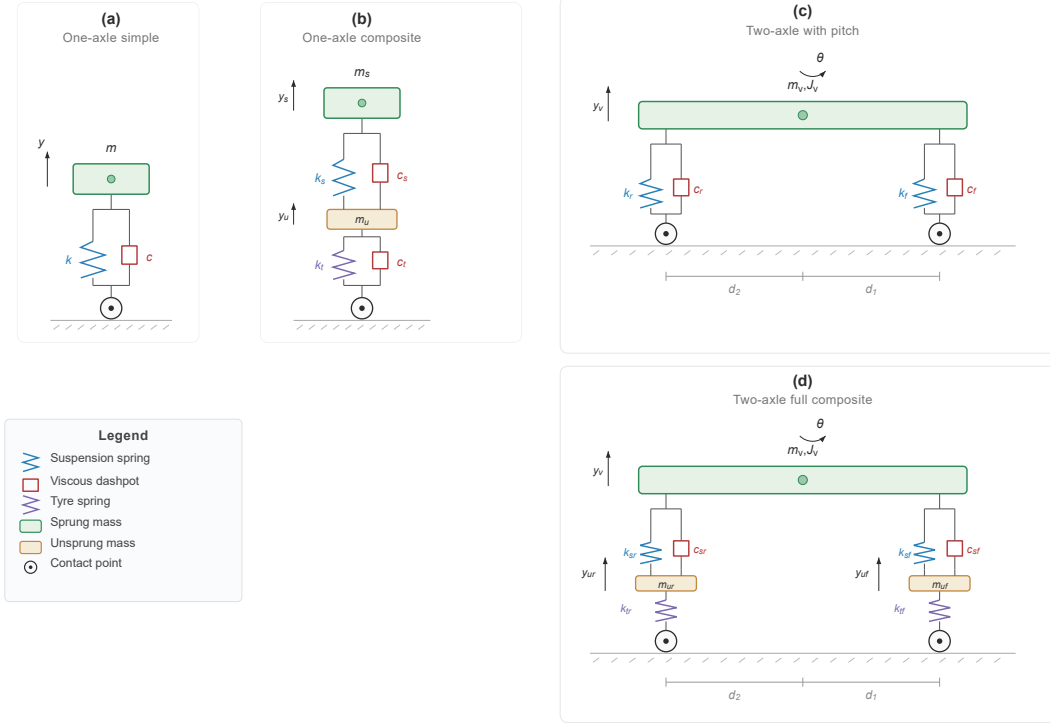


Figure 2: Vehicle models supported by the framework: (a) single-axle simple, (b) quarter-car composite, (c) half-car with pitch, and (d) full composite half-car with axle masses.

and the pitch equation is

$$\begin{aligned}
 J_v \ddot{\theta}_v + (d_1 c_f - d_2 c_r) \dot{\theta}_v + (d_1 k_f - d_2 k_r) \theta_v + (d_2^2 c_r + d_1^2 c_f) \dot{\theta}_v + (d_2^2 k_r + d_1^2 k_f) \theta_v \\
 = d_1 k_f u_{cf} - d_2 k_r u_{cr} + d_1 c_f \dot{u}_{cf} - d_2 c_r \dot{u}_{cr}
 \end{aligned} \tag{5}$$

This formulation, used by Yang et al. [5] in their VBI element, has two dynamic DOFs and two contact points. The rear contact force, for example, is $F_r = k_r(y_v - d_2 \theta_v - u_{cr}) + c_r(\dot{y}_v - d_2 \dot{\theta}_v - \dot{u}_{cr})$, with an analogous expression for the front.

The full composite half-car model (Figure 2 d) adds independent unsprung masses m_{ur} and m_{uf} at each axle, each with its own tyre assembly (k_{tr} , c_{tr} and k_{tf} , c_{tf}), giving four DOFs: two axle translations, body bounce, and pitch. This model captures the full dynamics of a two-axle truck, including the distinct frequency ranges of tyre hop ($\sim 10\text{--}15$ Hz) and body bounce ($\sim 1\text{--}3$ Hz), and has been used by OBrien et al. [8] and Cantero et al. [16].

2.3 Coupling Methods

The coupled VBI equations can be solved monolithically or through partitioned iteration. In the monolithic approach, the vehicle DOFs are incorporated directly into the beam element formulation; Yang’s VBI element [5,17] augments the standard beam element matrices with the vehicle’s mass, stiffness, and damping contributions evaluated at the current contact position. This yields an unconditionally stable solution without iteration but requires modification of the element library and reassembly of the global matrices at every time step.

The partitioned approach, adopted in this work, treats the bridge and vehicle as separate subsystems and exchanges forces and displacements through an external interface. Green and Cebon [6] described such a scheme for highway bridge dynamics, and Zhu and Law [7] extended it to multi-lane bridge decks. The approach is more modular (each subsystem can use its own solver, mesh, and time step) but requires iteration within each time step to enforce equilibrium and compatibility at the contact points. Convergence is measured by the relative change in the bridge displacement field between successive iterations:

$$\varepsilon^{(k)} = \frac{\sqrt{\frac{1}{N_n} \sum_{j=1}^{N_n} (w_j^{(k)} - w_j^{(k-1)})^2}}{\max_j |w_j^{(k)}|} < \epsilon_{\text{tol}} \quad (6)$$

where $w_j^{(k)}$ is the bridge displacement at node j in iteration k , N_n is the number of bridge nodes, and ϵ_{tol} is a user-specified tolerance (typically 10^{-4} to 10^{-12}).

2.4 Road Roughness

Road surface roughness is a primary excitation source for both the vehicle and the bridge in VBI problems. The ISO 8608 standard [18] characterises road profiles through their displacement power spectral density (PSD), which is modelled as a function of spatial frequency:

$$G_d(n) = G_d(n_0) \left(\frac{n}{n_0} \right)^{-w} \quad (7)$$

where n is the spatial frequency in cycles/m, $n_0 = 0.1$ cycles/m is the reference frequency, $w = 2$ is the waviness exponent, and $G_d(n_0)$ is the roughness coefficient that defines the road class. The ISO 8608 standard classifies road surfaces into categories A through E based on the value of $G_d(n_0)$, as summarised in Table 1.

Table 1: ISO 8608 road roughness classification at reference spatial frequency $n_0 = 0.1$ cycles/m. Roughness coefficients $G_d(n_0)$ in 10^{-6} m^3 .

Class	Description	Lower limit	Geometric mean	Upper limit
A	Very good	—	1	2
B	Good	2	4	8
C	Average	8	16	32
D	Poor	32	64	128
E	Very poor	128	256	512

A synthetic road roughness profile is generated as a sum of harmonics with random phase angles:

$$r(x) = \sum_{i=1}^{N_h} \sqrt{2 G_d(n_i) \Delta n} \cos(2\pi n_i x + \phi_i) \quad (8)$$

where ϕ_i are independent random phase angles uniformly distributed over $[0, 2\pi]$, Δn is the spatial frequency increment, and n_i ranges from a lower bound n_l to an upper bound n_u . In the implementation, $n_u = 10$ cycles/m captures wavelengths down to 0.1 m, while Δn is chosen such that the period of the roughness profile ($1/\Delta n$) exceeds at least twice the bridge span, preventing artificial periodicity within the analysis window.

2.5 Numerical Platforms for VBI

VBI simulations have been implemented in a wide range of numerical environments. Commercial finite element packages such as ABAQUS, ANSYS, and LS-DYNA support full-vehicle and bridge models but typically require user-written subroutines for iterative coupling, and their licensing restricts open sharing of benchmark configurations. Research codes, including the VBI-2D solver used to generate the NuBe dataset [22], provide well-documented reference results but are often tied to specific vehicle topologies or solver choices. Open-source structural analysis platforms such as OpenSees [15] (exposed in Python via OpenSeesPy [19]) offer reusable building blocks for structural dynamics but do not ship with native moving-mass analysis or direct coupling of separate bridge and vehicle subsystems. The present framework targets this gap: it builds on a widely used open-source platform and adds an external Python coupling layer that works with standard elements, so that complete VBI models and benchmark cases can be shared, inspected, and extended without modifying the underlying solver.

3 Methodology

3.1 Overview

The proposed framework analyses the VBI problem by constructing two independent OpenSees finite element models at each time step: one for the bridge and one for the vehicle. The bridge model is a standard Euler-Bernoulli beam discretised with `elasticBeamColumn` elements, while the vehicle model uses lumped masses and `zeroLength` spring-dashpot elements to represent the suspension and tyre assemblies. At each time step, the two models are coupled through the following iterative procedure: (i) the bridge deformation at the vehicle axle locations is interpolated and combined with the road roughness to form the vehicle input; (ii) the vehicle model is solved for one time step under this displacement excitation; (iii) the vehicle reaction forces are mapped back onto the bridge nodes; (iv) the bridge model is solved for one time step under the updated nodal forces; and (v) convergence is checked against the bridge displacement. This process is illustrated schematically in Figure 3 and Figure 4 (see also Figure 1 for the physical problem setup).

3.2 Bridge Finite Element Model

The bridge is modelled as a two-dimensional Euler-Bernoulli beam using OpenSees `elasticBeamColumn` elements in a 2D frame formulation with three degrees of freedom per node (two translations and one rotation). The bridge is discretised into N_e elements of uniform length $\Delta x = L/N_e$, producing $N_n = N_e + 1$ nodes. Lumped mass is assigned to each node proportional to the tributary length: interior nodes receive $\bar{m}\Delta x$ and the two end nodes receive $\bar{m}\Delta x/2$, where \bar{m} is the mass per unit length. Boundary conditions are applied at the support nodes: the first support is modelled as a pin (fixed in x and y , free in rotation), and subsequent supports are modelled as rollers (fixed in y only). Multi-span continuous bridges are supported by specifying the locations of intermediate supports.

Rayleigh damping is applied using the mass-proportional and committed-stiffness-proportional coefficients computed from the target damping ratio ζ and the first two natural frequencies:

$$\alpha_M = \zeta \frac{2\omega_1\omega_2}{\omega_1 + \omega_2}, \quad \beta_K = \frac{2\zeta}{\omega_1 + \omega_2} \quad (9)$$

where ω_1 and ω_2 are the first two circular natural frequencies obtained from an eigenvalue analysis of the bridge model. Time integration is performed using the Newmark method [20] with parameters $\gamma = 0.5$ and $\beta = 0.25$ (constant average acceleration), which provides unconditional stability [21].

At each time step, the bridge model is rebuilt from scratch in OpenSees (after a `wipe` command), the initial conditions from the previous step are imposed using `setNodeDisp`, `setNodeVel`, and `setNodeAccel`, the nodal force time series is applied, and a single transient analysis step is performed. This rebuild-per-step strategy eliminates the need to maintain persistent state within OpenSees and enables straightforward implementation of the iterative coupling without conflicts between vehicle and bridge model definitions.

3.3 Vehicle Finite Element Models

The framework implements the four vehicle model types described in Section 2 (see Figure 2). All vehicle models are constructed in OpenSees using lumped masses at the DOF nodes and `zeroLength` or `twoNodeLink` elements with elastic materials to represent springs and dashpots. For all vehicle models, the axle (wheel) nodes are constrained as fixed supports in the OpenSees model. At each time step, both the displacement and velocity at each axle are prescribed using OpenSees' `MultipleSupport` pattern with `imposedMotion`, where the displacement time series is the sum of the interpolated bridge deformation and the road roughness at the axle location, and the velocity time series is the corresponding time derivative. This combined displacement-velocity excitation ensures that the Newmark integrator receives consistent kinematic input, avoiding spurious accelerations that would arise from differencing displacement alone. The reaction forces at the axle nodes, obtained via OpenSees' `nodeReaction` command with the `-dynamic` and `-rayleigh` flags, represent the total dynamic contact force between the vehicle and the bridge.

For the quarter-car models (simple and composite), the OpenSees model is constructed in one dimension (`ndm=1`), with the axle node fixed and the body and axle masses connected by `zeroLength` spring-dashpot elements. For the half-car models with body pitch (`comp2` and `comp3`), a 2D frame formulation (`ndm=2`, `ndf=3`) is required to represent the rotational DOF. The body centre of gravity is modelled as a node carrying the body mass and the pitch moment of inertia, connected to the suspension attachment points above each axle through very stiff penalty elements (`twoNodeLink` with stiffness $\sim 10^6 \times k_s$). These penalty links enforce near-rigid-body kinematics between the CG node and the suspension tops, so that body bounce and pitch are transmitted to the axle positions through the suspension springs without introducing additional

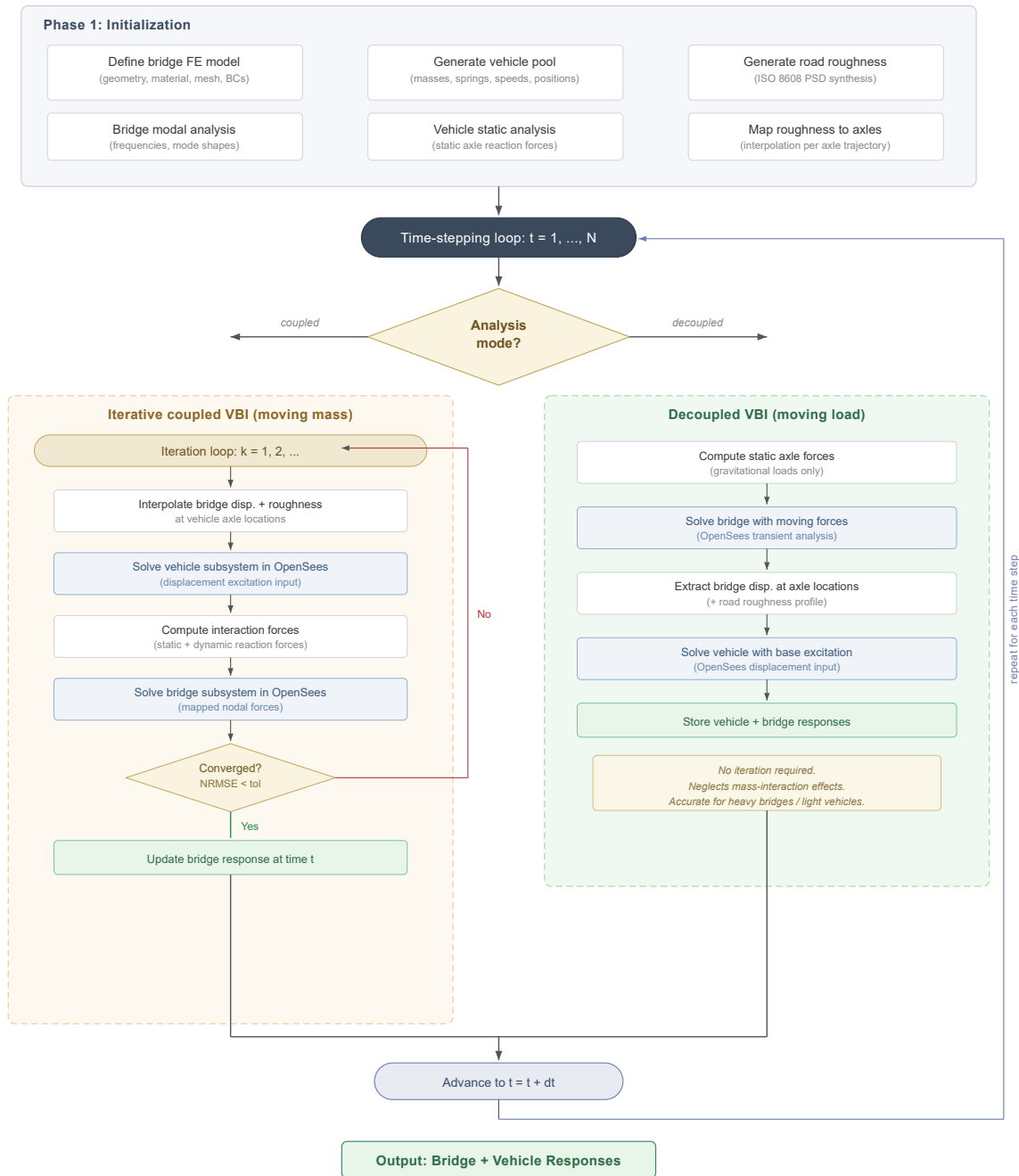


Figure 3: Framework flowchart showing the complete analysis procedure, including initialisation, the time-stepping loop, and the two analysis modes (coupled iterative and decoupled moving load).

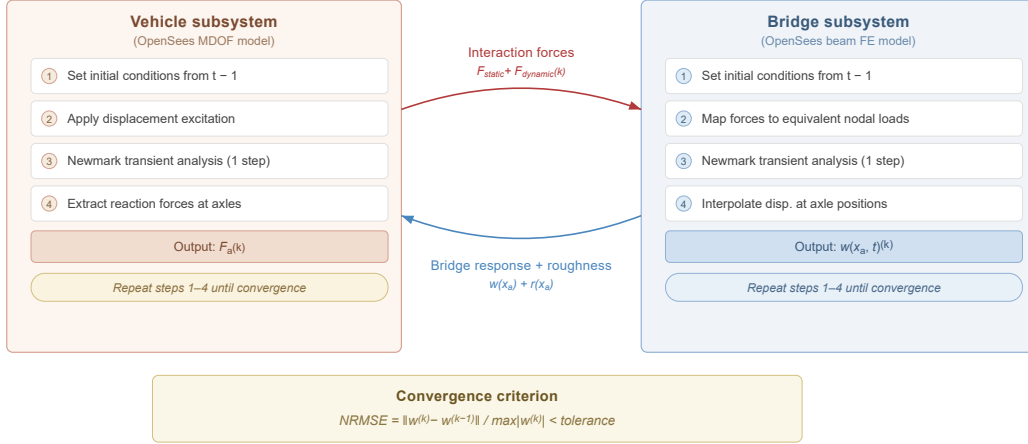


Figure 4: Iterative partitioned coupling scheme at a single time step, showing the exchange of displacement and force quantities between the vehicle and bridge subsystems.

flexible modes. Table 6 in the Appendix gives the complete node and element connectivity for each vehicle model type.

A static analysis is performed once at the beginning of the simulation to determine the static axle forces under gravity. These forces represent the baseline moving load that acts on the bridge even in the absence of dynamic effects.

3.4 Force Mapping

The vehicle contact forces must be mapped from the axle positions (which generally do not coincide with bridge nodes) onto the nearest bridge nodes. Linear shape function interpolation is used: for an axle located at position x_a within element $[x_i, x_{i+1}]$ of length ℓ , the force F_a is distributed to the two element nodes as

$$F_i = \left(1 - \frac{x_a - x_i}{\ell}\right) F_a, \quad F_{i+1} = \frac{x_a - x_i}{\ell} F_a \quad (10)$$

where x_i and x_{i+1} are the coordinates of the element end nodes. This linear interpolation is consistent with the linear (Hermitian) displacement interpolation within a beam element and ensures that the total force and its first moment are preserved. When an axle is located outside the bridge span (i.e., before entering or after exiting the bridge), its force contribution is excluded from the bridge loading.

3.5 Iterative Coupling Algorithm

The complete iterative coupling procedure at time step t_{n+1} is formalised in Algorithm 1.

Algorithm 1 Iterative Coupled VBI Analysis at Time Step t_{n+1}

Require: Bridge state at t_n : $\{w_n, \dot{w}_n, \ddot{w}_n\}$; Vehicle state at t_n ; Road roughness $r(x)$

Ensure: Updated bridge and vehicle states at t_{n+1}

```

1: Initialise  $w_{n+1}^{(0)}$  from the free-vibration bridge response (no vehicle forces)
2: Set iteration counter  $k \leftarrow 0$ 
3: repeat
4:    $k \leftarrow k + 1$ 
5:   for each vehicle  $v$  do
6:     for each axle  $i$  of vehicle  $v$  do
7:       Compute axle position:  $x_{a,i} = x_{\text{rear}}(t_{n+1}) + d_i$ 
8:       Interpolate bridge displacement and velocity at  $x_{a,i}$ 
9:       Compute axle displacement:  $u_i = w_b(x_{a,i}) + r(x_{a,i})$ 
10:      Compute axle velocity:  $\dot{u}_i = \dot{w}_b(x_{a,i}) + \dot{r}(x_{a,i})$ 
11:    end for
12:    Solve vehicle FE model with imposed displacement  $\{u_i\}$  and velocity  $\{\dot{u}_i\}$ 
13:    Extract axle reaction forces  $\{F_{a,i}\}$  via nodeReaction(-dynamic, -rayleigh)
14:  end for
15:  Initialise nodal force vector:  $F_{\text{inter}} \leftarrow 0$ 
16:  for each vehicle  $v$ , each axle  $i$  do
17:     $F_{\text{total},i} \leftarrow F_{\text{static},i} + F_{a,i}^{\text{dynamic}}$ 
18:    if  $F_{\text{total},i} > 0$  then ▷ Check for wheel uplift
19:      Map  $F_{\text{total},i}$  to bridge nodes using @eq-force-mapping
20:    end if
21:  end for
22:  Add background traffic force:  $F_n \leftarrow F_{\text{traffic}} + F_{\text{inter}}$ 
23:  Solve bridge FE model in OpenSees with nodal forces  $F_n$ 
24:  Extract updated bridge response  $w_{n+1}^{(k)}$ 
25:  Compute convergence residual  $\varepsilon^{(k)}$  using Equation 6
26: until  $\varepsilon^{(k)} < \epsilon_{\text{tol}}$ 
27: Store converged bridge and vehicle states at  $t_{n+1}$ 

```

The convergence tolerance on the bridge displacement residual $\varepsilon^{(k)}$ (Equation 6) is set to $\epsilon_{\text{tol}} = 10^{-12}$ for all validation studies in this paper. In practice, values of 10^{-4} to 10^{-6} are sufficient for engineering accuracy. The algorithm typically converges in one to four iterations per time step for typical vehicle-to-bridge mass ratios.

3.6 Simplified Decoupled Approach

For situations where the vehicle mass is small relative to the bridge mass, or when computational efficiency is paramount, the framework provides a simplified decoupled (non-iterative) analysis mode. This approach is summarised in Algorithm 2.

Algorithm 2 Decoupled VBI Analysis (Moving Load + Base Excitation)

Require: Bridge properties; Vehicle properties; Road roughness $r(x)$; Vehicle trajectory $x(t)$

Ensure: Bridge and vehicle response histories

- 1: Compute vehicle static axle forces $\{F_{\text{static},i}\}$
 - 2: for each time step t_n do
 - 3: Compute axle positions $\{x_{a,i}(t_n)\}$
 - 4: Map static forces to bridge nodes using @eq-force-mapping
 - 5: end for
 - 6: Solve bridge FE model for all time steps under mapped static forces
 - 7: Extract bridge displacement history at all nodes: $w(x, t)$
 - 8: for each vehicle v , each axle i , each time step t_n do
 - 9: Interpolate bridge displacement and velocity at axle position $x_{a,i}(t_n)$
 - 10: $u_i(t_n) = w_b(x_{a,i}, t_n) + r(x_{a,i}(t_n)); \quad \dot{u}_i(t_n) = \dot{w}_b(x_{a,i}, t_n) + \dot{r}(x_{a,i}(t_n))$
 - 11: end for
 - 12: Solve vehicle FE model with imposed displacement and velocity histories $\{u_i(t), \dot{u}_i(t)\}$
-

The decoupled approach neglects the feedback of the vehicle’s dynamic forces on the bridge, treating the vehicle purely as a constant moving load. This is equivalent to ignoring the inertial coupling between the vehicle and bridge subsystems. The approach is exact in the limit of zero vehicle mass (moving force problem) and becomes increasingly approximate as the vehicle-to-bridge mass ratio increases. Its principal advantage is computational efficiency: the bridge needs to be solved only once (rather than iteratively at each time step), and the vehicle can also be solved in a single pass using the precomputed bridge response as input.

3.7 Road Roughness Generation

Road roughness profiles are generated according to the ISO 8608 spectral model described in Equation 7 and Equation 8. The spatial frequency range is set from n_l to n_u with increment Δn . The generated profile is optionally smoothed with a moving average filter to attenuate unrealistically high-frequency components that arise from the finite harmonic summation. The roughness profile extends over the full analysis window, which includes approach roads before and after the bridge span, ensuring that the vehicle suspension is excited by road roughness before it enters the bridge.

The roughness input to each axle accounts for the spatial lag between axles. For a vehicle with axles at local coordinates $\{d_0, d_1, \dots, d_{N_a-1}\}$ relative to the rear axle and a rear axle position history $x_{\text{rear}}(t)$, the roughness input to axle i at time t is $r(x_{\text{rear}}(t) + d_i)$.

4 Validation

This section validates the framework against established benchmark configurations from the VBI literature, covering three levels of vehicle model complexity and two independent reference sources.

4.1 Benchmark 1: Quarter-Car Vehicle [2]

The first benchmark reproduces the configuration from Yang et al. [2], who analysed a quarter-car spring-mass vehicle traversing a simply supported beam. The vehicle and bridge parameters are listed in Table 2.

Table 2: Bridge and vehicle parameters for Benchmark 1 [2].

Parameter	Symbol	Value	Unit
Bridge			
Span length	L	25	m
Elastic modulus	E	2.75×10^{10}	Pa
Second moment of area	I	0.12	m^4
Cross-sectional area	A	2.0	m^2
Mass per unit length	\bar{m}	4800	kg/m
Damping ratio	ζ	0	—
Vehicle			
Sprung mass	m_v	1200	kg
Suspension stiffness	k_v	5.0×10^5	N/m
Suspension damping	c_v	0	N s/m
Speed	v	10	m/s

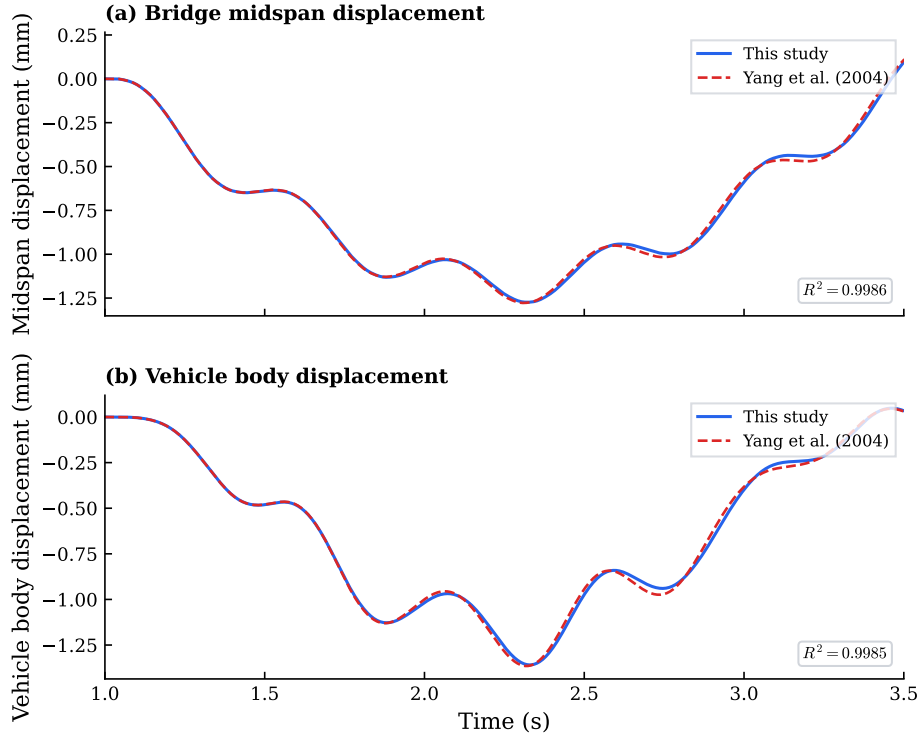


Figure 5: Benchmark 1: this study (solid blue) and Yang et al. (2004) benchmark (dashed red) for a quarter-car vehicle traversing a 25 m simply supported beam [2]. (a) Bridge midspan displacement; (b) vehicle body displacement.

Figure 5 compares this study with the Yang et al. [2] quarter-car benchmark. Agreement between the two curves is quantified using the coefficient of determination

$$R^2 = 1 - \frac{\sum_n (y_s(t_n) - y_b(t_n))^2}{\sum_n (y_s(t_n) - \bar{y}_s)^2}, \quad (11)$$

where y_s and y_b are the present-study and benchmark histories and \bar{y}_s is the mean of y_s over the on-bridge window; R^2 approaches unity when the two signals coincide. For this benchmark, R^2 exceeds 0.998 for both bridge midspan and vehicle body displacement (annotated on Figure 5), consistent with the visual overlap. The vehicle mass (1200 kg) is small relative to the bridge mass ($4800 \text{ kg/m} \times 25 \text{ m} = 120,000 \text{ kg}$), yielding

a mass ratio of 1%. The bridge fundamental frequency (2.08 Hz) and the vehicle frequency (3.25 Hz) are well separated, and the response is dominated by the first beam mode.

4.2 Benchmark 2: Half-Car Vehicle with Pitch [5]

The second benchmark increases the vehicle model complexity by using the half-car asymmetric vehicle with body pitch from Yang et al. [5]. The vehicle and bridge parameters are listed in Table 3.

Table 3: Bridge and vehicle parameters for Benchmark 2 [5].

Parameter	Symbol	Value	Unit
Bridge			
Span length	L	30	m
Flexural rigidity	EI	1.56×10^{10}	N m ²
Mass per unit length	\bar{m}	4400	kg/m
Damping ratio	ζ	0	—
Vehicle			
Body mass	m_v	2500	kg
Pitch moment of inertia	J_v	2300	kg m ²
Front suspension stiffness	k_f	2.3×10^5	N/m
Rear suspension stiffness	k_r	1.8×10^5	N/m
Front suspension damping	c_f	0	N s/m
Rear suspension damping	c_r	0	N s/m
Axle spacing	d	3	m
CG to rear axle	d_1	1.7	m
Speed	v	10	m/s

Figure 6 compares this study with the Yang et al. [5] half-car benchmark with body pitch. The vehicle mass (2500 kg) relative to the bridge mass ($4400 \text{ kg/m} \times 30 \text{ m} = 132,000 \text{ kg}$) yields a mass ratio of approximately 1.9%. The maximum midspan displacement of approximately 0.85 mm occurs when the vehicle is near the centre of the span, and the response exhibits a multi-modal character due to the asymmetric half-car loading. The vehicle body displacement and pitch rotation closely follow the Yang et al. (2019) benchmark, including near pitch-response peaks. The pitch rotation grows in amplitude as the vehicle traverses the span, reflecting the increasing excitation of the pitching mode by the offset centre of gravity.

4.3 Benchmark 3: NuBe Vehicle Models [16]

The third benchmark uses vehicle and bridge configurations from the NuBe numerical benchmark dataset [16], which provides a standardised set of VBI simulation results generated using the independent VBI-2D MATLAB solver [22]. We configure our framework with the mean vehicle properties from the NuBe V1 (quarter-car) and V2 (half-car with pitch) models and run them on the NuBe B27 bridge (27 m span). The bridge and vehicle parameters are listed in Table 4.

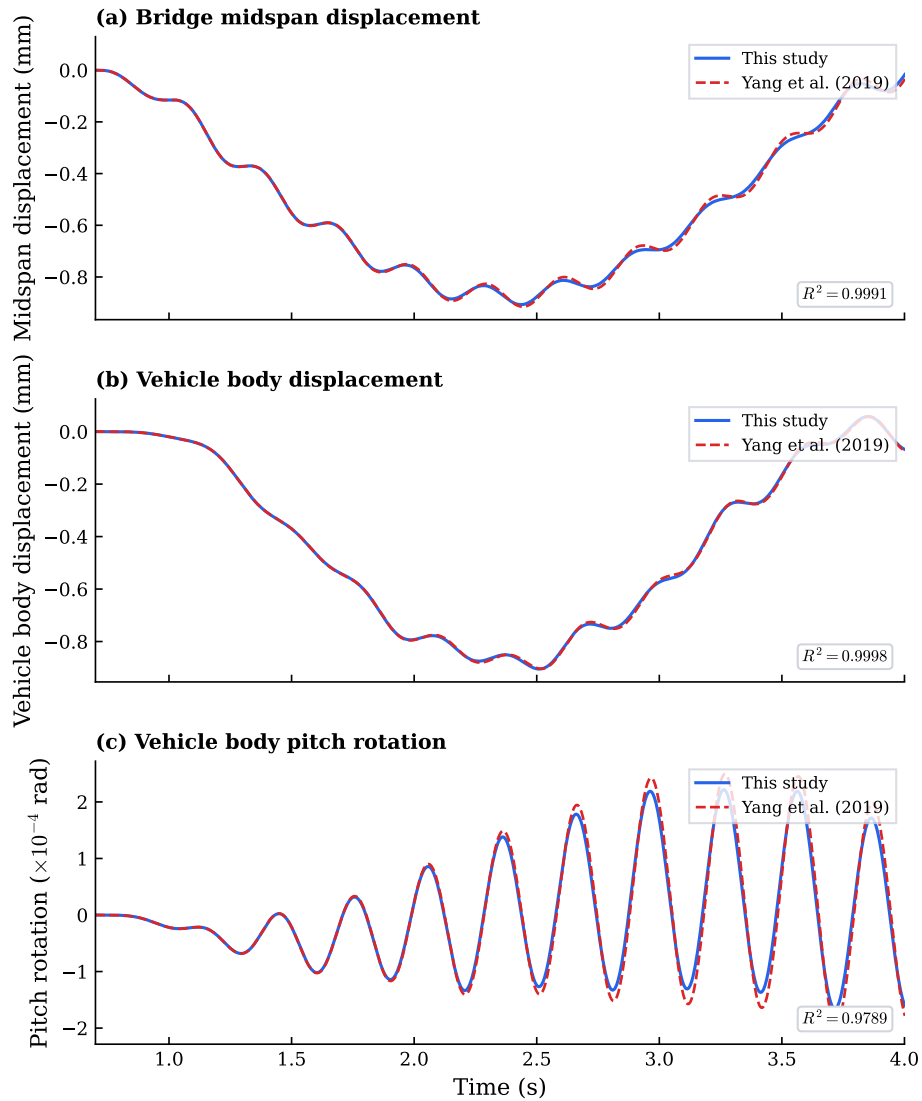


Figure 6: Benchmark 2: this study (solid blue) and Yang et al. (2019) benchmark (dashed red) for a half-car vehicle with pitch traversing a 30 m simply supported beam [5]. (a) Bridge midspan displacement; (b) vehicle body displacement; (c) vehicle body pitch rotation.

Table 4: Bridge and vehicle parameters for Benchmark 3, using mean values from the NuBe dataset [16].

Parameter	Symbol	Value	Unit
Bridge (B27)			
Span length	L	27	m
Young’s modulus	E	3.5×10^{10}	Pa
Second moment of area	I	1,7055	m ⁴
Mass per unit length	\bar{m}	19,372	kg/m
Damping ratio	ζ	0	—
First natural frequency	f_1	3.7824	Hz
Vehicle V1 (quarter-car)			
Body mass	m_B	8,000	kg
Axle mass	m_G	1,100	kg
Suspension stiffness	k_S	2.0×10^6	N/m
Suspension damping	c_S	4.0×10^4	N s/m
Tyre stiffness	k_T	3.5×10^6	N/m
Speed	v	25	m/s
Vehicle V2 (half-car)			
Body mass	m_{B1}	10,500	kg
Axle mass (each)	m_G	900	kg
Body moment of inertia	I_{B1}	50,000	kg m ²
Suspension stiffness (each)	k_S	6.0×10^6	N/m
Suspension damping (each)	c_S	1.0×10^4	N s/m
Tyre stiffness (each)	k_T	1.75×10^6	N/m
Axle spacing	d	5.0	m
Speed	v	25	m/s

The NuBe benchmark exercises two vehicle model types on the same bridge, testing both the single-axle composite (quarter-car) and the full two-axle composite (half-car with pitch and independent axle masses). The V1 quarter-car model (total mass 9,100 kg, mass ratio $\mu \approx 1.7\%$) produces a smooth midspan deflection dominated by the first beam mode. The V2 half-car model (total mass 12,300 kg, $\mu \approx 2.4\%$) introduces a richer response due to the pitching motion and the separate excitation of two contact points. For both vehicles, the coupled and decoupled analyses agree closely, consistent with the low mass ratios. The ability to reproduce the NuBe configurations using standard vehicle parameters from an independent benchmark dataset [16] confirms the interoperability of the proposed framework with established VBI simulation tools.

4.4 Benchmark 4: Convergence and Iteration Behaviour

The convergence behaviour of the iterative algorithm is examined for the Yang et al. (2019) half-car configuration [5] from Section 4.2.

The iteration count ranges from 1 to 4 across the time steps, with the majority of steps (approximately 60%) requiring 4 iterations and most of the remainder converging in 1–2 iterations at the tight tolerance of 10^{-12} . The iteration count is highest during the on-bridge portion and drops as the vehicle exits. This rapid convergence confirms the effectiveness of the iterative partitioned scheme for typical VBI problems.

5 Parametric Study: Coupled vs. Decoupled Analysis

This section quantifies the conditions under which the computationally efficient decoupled approach provides acceptable accuracy compared to the fully coupled iterative analysis. The key parameter governing the accuracy of the decoupled approach is the vehicle-to-bridge mass ratio $\mu = m_v/(\bar{m}L)$, where m_v is the total vehicle mass and $\bar{m}L$ is the total bridge mass. When $\mu \ll 1$, the vehicle’s inertial effect on the bridge is negligible and the decoupled approach is accurate; as μ increases, the interaction becomes significant and the coupled approach is necessary. The study considers four simply supported bridge spans with realistic cross-section properties, two quarter-car vehicle models spanning more than an order of magnitude in mass, six vehicle speeds, three ISO 8608 roughness classes, and varying levels of background traffic. The bridge and vehicle configurations follow those of Eshkevari et al. [12].

Table 5 lists the bridge configurations used in this section. The second moment of area I is computed from the reported box cross-section dimensions, and the mass per unit length \bar{m} is calibrated to match the fundamental

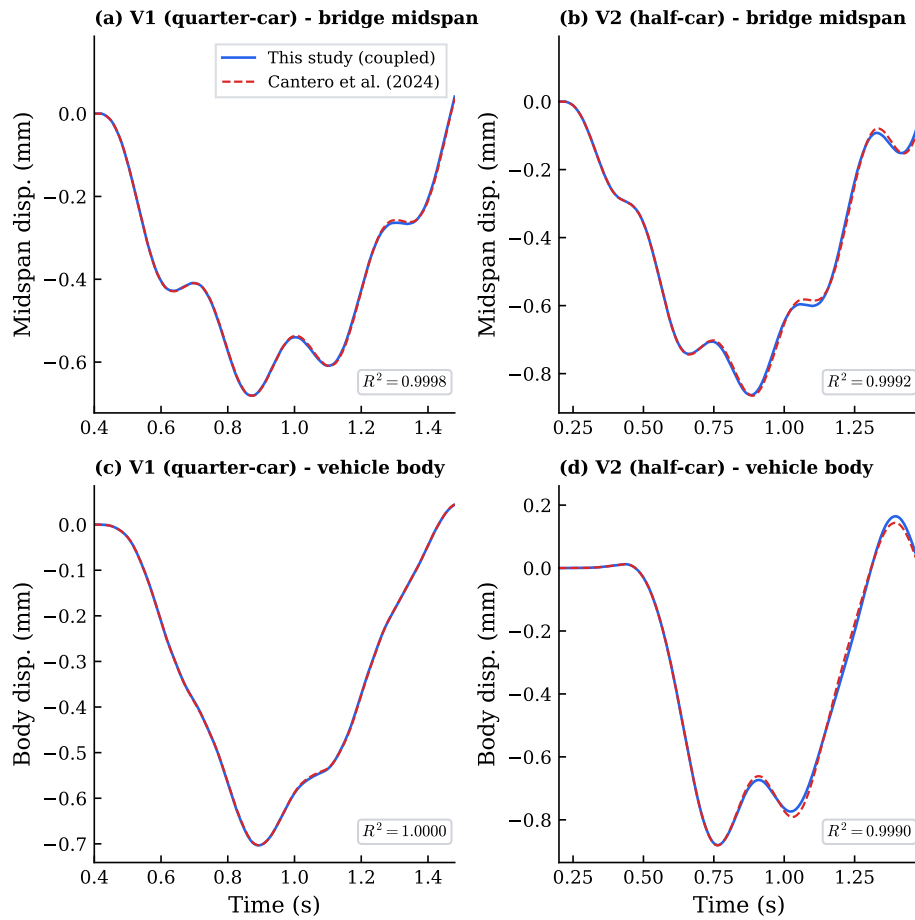


Figure 7: Benchmark 3: bridge midspan displacement and vehicle body response for the NuBe V1 (quarter-car) and V2 (half-car) models on the B27 bridge (27 m, undamped, smooth road). Solid lines: coupled iterative analysis; dashed lines: decoupled moving load approach.

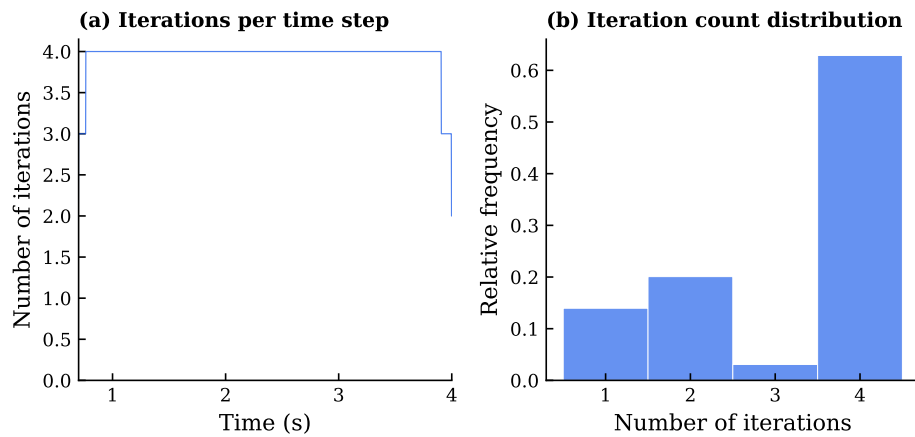


Figure 8: Convergence characteristics of the iterative coupling algorithm: (a) number of iterations per time step for the Yang et al. (2019) configuration; (b) iteration count distribution showing convergence in 1–4 iterations per time step.

frequency of each span using the Euler-Bernoulli simply supported beam formula $f_1 = (\pi/2L^2)\sqrt{EI/\bar{m}}$ with $E = 27.5$ GPa. The resulting \bar{m} values represent the equivalent distributed mass of the full bridge deck, including slab, parapets, and wearing surface. Two quarter-car vehicle models are used: the commercial vehicle (total mass 535.9 kg) and the heavy truck (total mass 18,000 kg) from Eshkevari et al. [12]. All analyses use ISO 8608 Class C road roughness, 0.3% Rayleigh damping, and a constant vehicle speed of 10 m/s. The spatial frequency increment for roughness generation is set to $\Delta n = \min(0.01, 1/(2L))$ cycles/m to ensure that the fundamental period of the synthesised profile exceeds twice the bridge length, avoiding artificial periodicity for longer spans.

Table 5: Bridge configurations for the parametric study, adapted from Eshkevari et al. The second moment of area I is computed from the box cross-section dimensions; the mass per unit length \bar{m} is calibrated to match the target fundamental frequency.

Span (m)	Depth (m)	Width (m)	t_f (m)	t_w (m)	I (m ⁴)	\bar{m} (kg/m)	f_1 (Hz)	μ_{comm}	μ_{heavy}
15	0.60	0.30	0.04	0.02	0.0024	49	8.03	0.7303	24.530
30	1.10	0.50	0.05	0.03	0.0188	119	3.63	0.1495	5.022
50	1.60	1.30	0.10	0.05	0.1693	437	2.05	0.0245	0.823
100	2.40	2.00	0.15	0.10	0.9148	1104	0.75	0.0049	0.163

5.1 Effect of Bridge Span Length

The first investigation varies the bridge span from 15 m to 100 m while keeping the vehicle, roughness, and speed parameters fixed. Both vehicle types are tested on each bridge to simultaneously capture the effects of span length and vehicle mass.

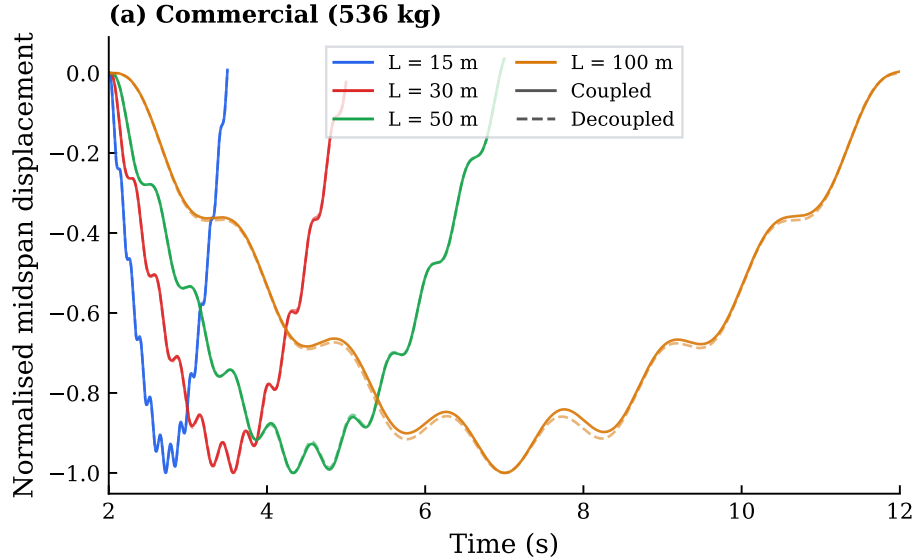


Figure 9: Normalised bridge midspan displacement for the commercial vehicle across four spans (15 m, 30 m, 50 m, 100 m). Solid lines: coupled iterative analysis. Dashed lines: decoupled (moving load) analysis.

The results reveal a clear separation between the two vehicle classes. For the commercial vehicle ($m_v \approx 536$ kg), the coefficient of determination R^2 between coupled and decoupled bridge displacement remains above 0.999 across all four spans, confirming that a vehicle of this mass has negligible inertial effect on any of the bridges tested (Figure 11). For the heavy truck ($m_v \approx 18,000$ kg), the agreement deteriorates markedly: at the 15 m span ($\mu \approx 24.5$, where the truck outweighs the bridge), R^2 drops well below unity, and even at the 100 m span ($\mu \approx 0.16$) it remains noticeably below the commercial-vehicle value. The vehicle body acceleration R^2 (Figure 12) follows the same qualitative pattern with an even larger gap between the two vehicles, reflecting the amplification of interaction effects through the suspension dynamics.

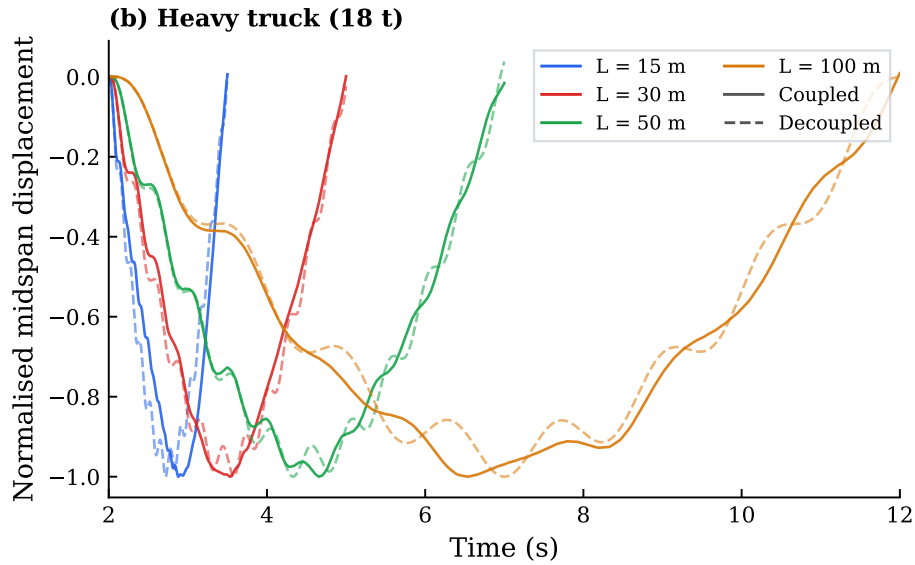


Figure 10: Normalised bridge midspan displacement for the heavy truck across four spans. Solid lines: coupled iterative analysis. Dashed lines: decoupled (moving load) analysis.

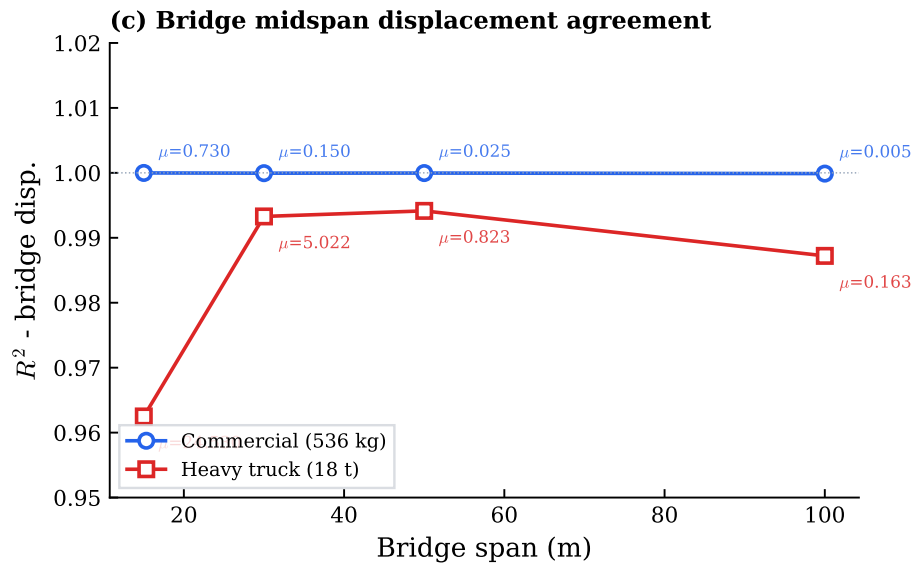


Figure 11: Coefficient of determination R^2 for bridge midspan displacement between coupled and decoupled analyses as a function of span length, for the commercial vehicle (blue circles) and the heavy truck (red squares). Mass ratios μ are annotated next to each data point. Values close to 1 indicate close agreement.

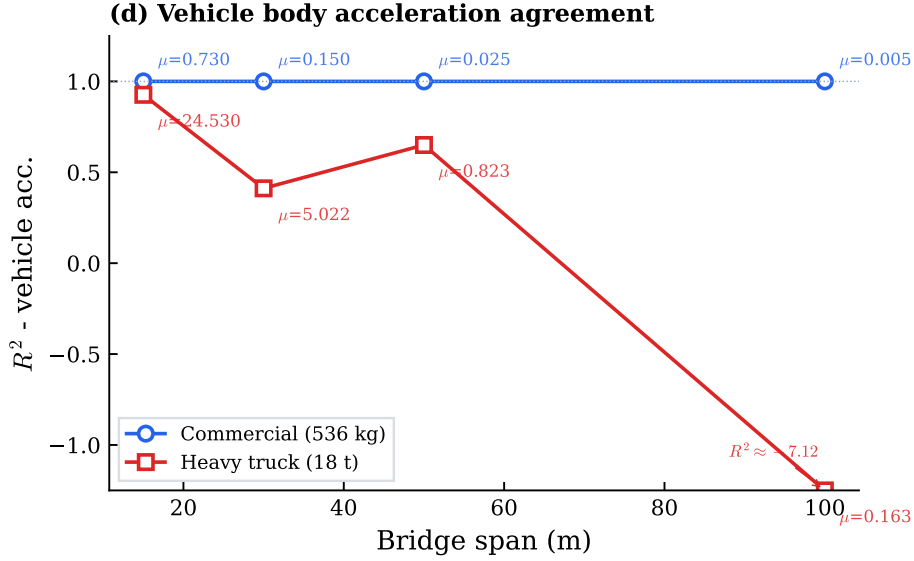


Figure 12: Coefficient of determination R^2 for vehicle body acceleration between coupled and decoupled analyses as a function of span length, for the commercial vehicle and the heavy truck.

A noteworthy feature of Figure 12 is that the vehicle body acceleration R^2 drops sharply and becomes strongly negative for the heavy truck at the longest span ($L = 100$ m, $\mu \approx 0.163$, $R^2 \approx -7$), while the commercial vehicle at a similarly small mass ratio ($\mu \approx 0.005$ at $L = 100$ m) remains at $R^2 > 0.9999$. The two data points sit at the same end of the span axis but the two vehicle classes behave differently. This is a well-known property of the coefficient of determination when applied to low-variance signals, not a sign that the decoupled approximation has suddenly collapsed. Recall that R^2 normalises the coupled-vs-decoupled residual by the variance of the coupled signal about its mean, i.e. by $\sum_n (y_c - \bar{y}_c)^2$. At long spans the bridge fundamental frequency is very low (0.75 Hz for $L = 100$ m in the Eshkevari set) and the bridge-induced vehicle body acceleration is small, so the mean-centred variance $\sum_n (y_c - \bar{y}_c)^2$ becomes small. For the heavy truck this small denominator is combined with a residual coupling effect that is still non-negligible because the truck carries enough inertia to feed energy back into the bridge; the numerator $\sum_n (y_c - y_d)^2$ therefore dominates the denominator and pushes R^2 strongly negative, indicating only that the decoupled prediction is farther from the coupled signal than a constant equal to the coupled mean. It does not imply a large absolute error: the underlying RMS difference is still a small fraction of the bridge’s static moving-load response. For the commercial vehicle, the residual coupling effect is negligibly small because the vehicle mass is minute compared with the bridge mass, so the numerator collapses faster than the denominator and R^2 remains essentially unity. The same degenerate behaviour does not appear in the bridge midspan displacement (Figure 11), because bridge displacement has a dominant quasi-static component and hence a much larger $\sum_n (y_c - \bar{y}_c)^2$, so the denominator never collapses.

These results demonstrate that the mass ratio μ is the primary predictor of decoupled accuracy: for the lightweight commercial vehicle ($\mu < 1$), the decoupled approach is adequate regardless of span, while for heavy vehicles ($\mu > 0.1$), coupled analysis is necessary across all spans tested.

5.2 Effect of Vehicle Speed

This investigation examines the effect of vehicle speed on both bridge and vehicle responses using the 30 m bridge and the commercial quarter-car vehicle under Class A roughness. The vehicle speed is varied from 5 to 30 m/s (18 to 108 km/h), covering the typical range of highway traffic.

The vehicle speed governs the loading frequency seen by the bridge: faster vehicles excite higher-frequency content and spend less time on the span. At lower speeds (5–10 m/s), the bridge midspan displacement approaches the quasi-static deflection, with the response dominated by the first beam mode (Figure 13). As speed increases, dynamic amplification becomes apparent: the peak midspan displacement and the free-vibration oscillations after the vehicle exits grow with speed. The bridge midspan acceleration (Figure 14) increases markedly with speed, as the moving load excites the bridge at higher frequencies. The vehicle body

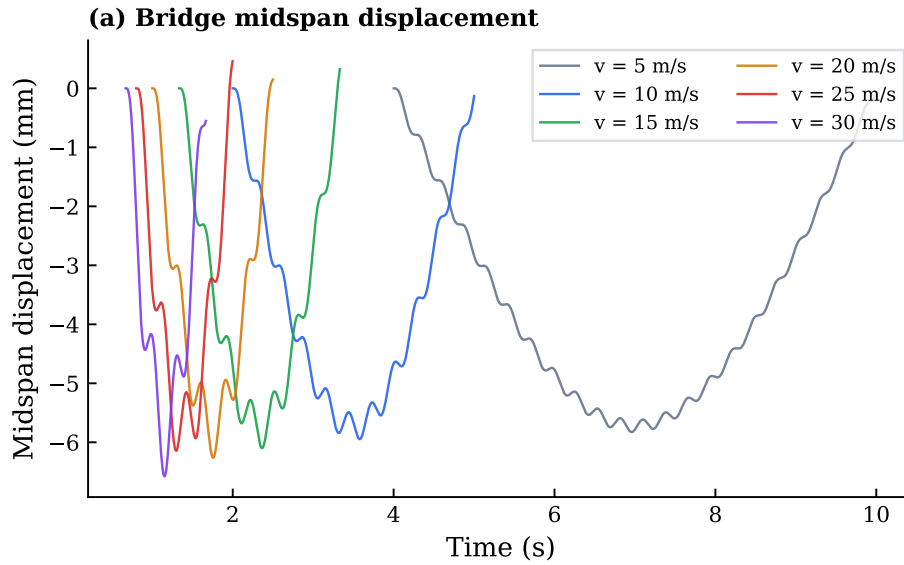


Figure 13: Bridge midspan displacement for the 30 m bridge under the commercial quarter-car vehicle at six vehicle speeds (5, 10, 15, 20, 25, 30 m/s), Class A roughness.

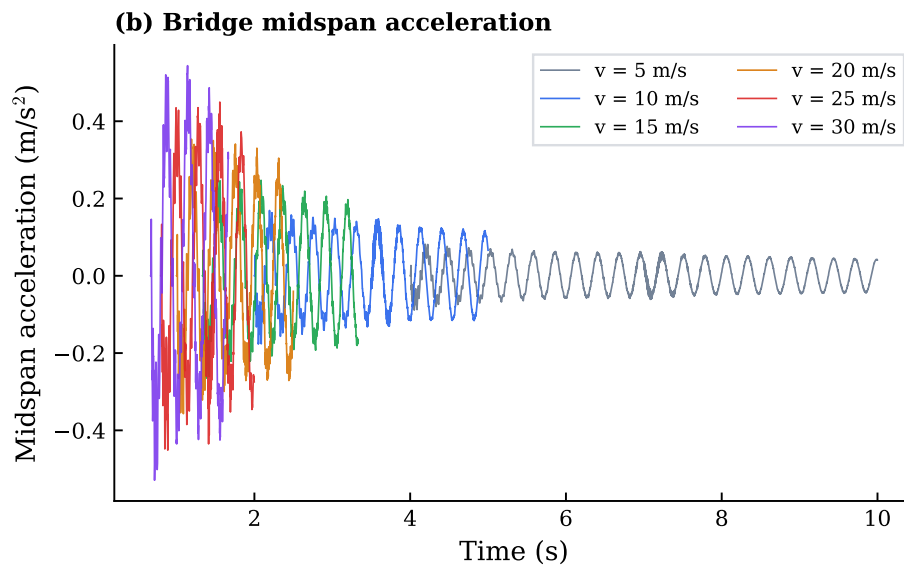


Figure 14: Bridge midspan acceleration for the same six vehicle speeds.

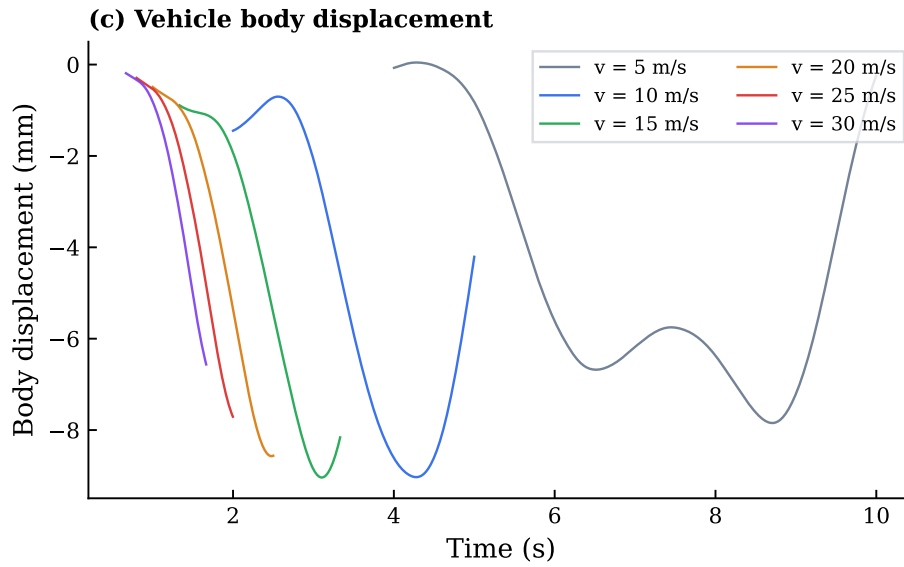


Figure 15: Vehicle body vertical displacement for the same six vehicle speeds.

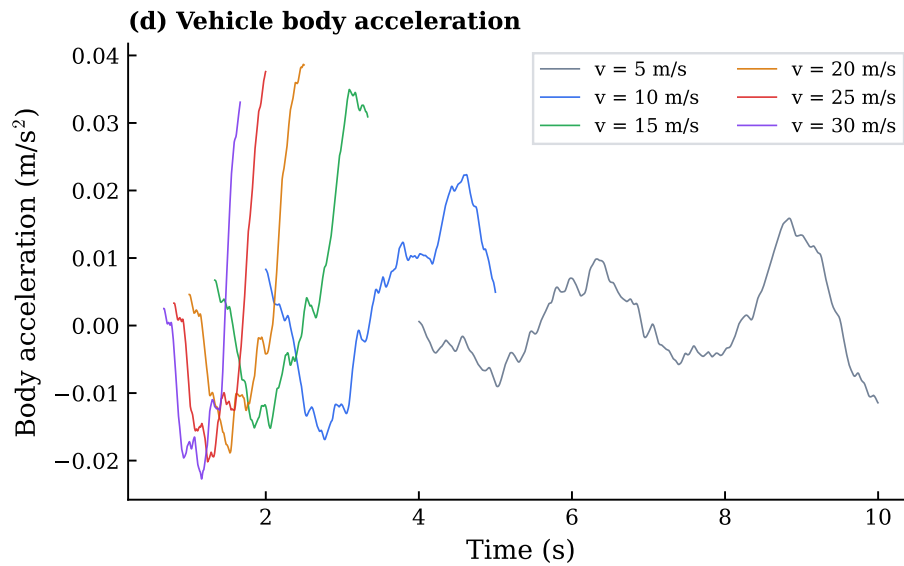


Figure 16: Vehicle body vertical acceleration for the same six vehicle speeds.

displacement (Figure 15) shows a similar trend, with higher speeds producing larger oscillations due to the more rapid traversal of the bridge deflection profile. The vehicle body acceleration (Figure 16) also increases with speed, reflecting the combined effect of dynamic bridge response and the higher-frequency roughness excitation at elevated velocities.

5.3 Road Roughness Effects

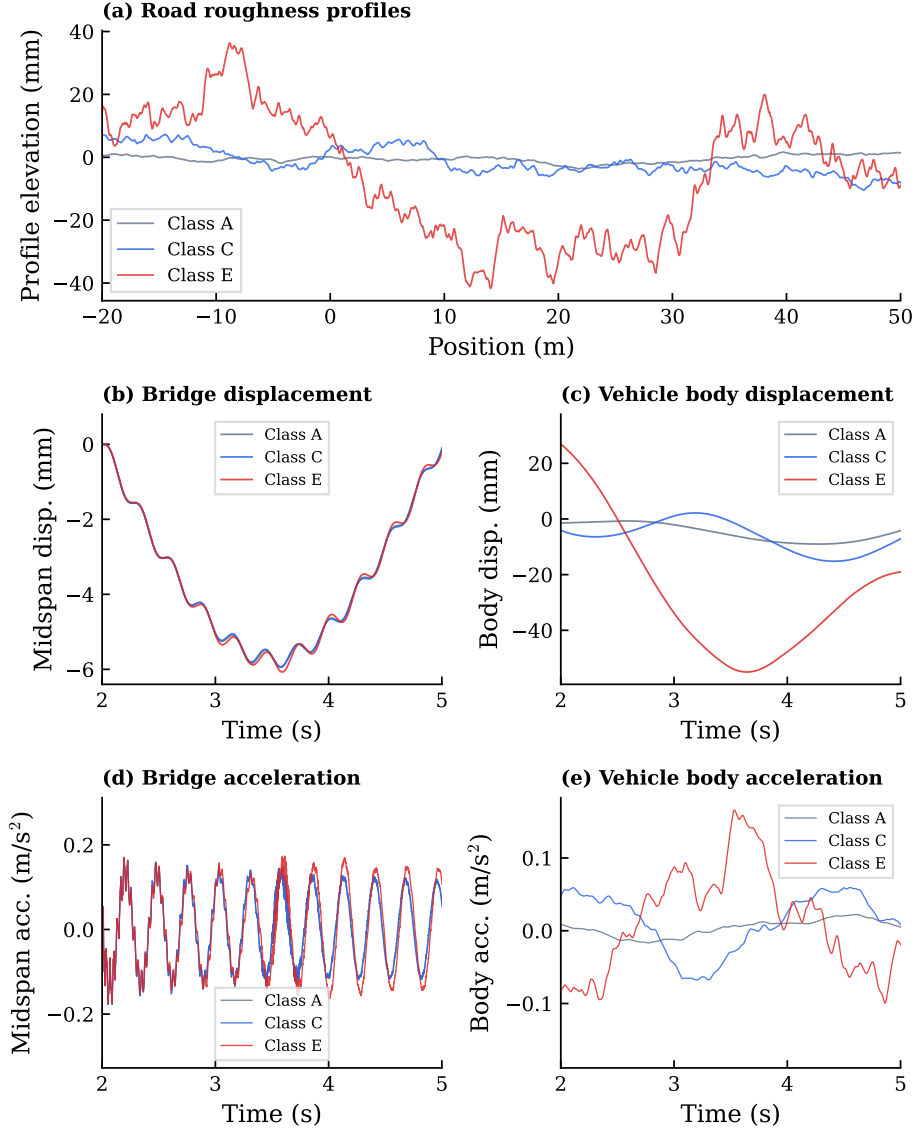


Figure 17: Effect of road roughness on bridge and vehicle response (30 m bridge, commercial quarter-car vehicle). (a) ISO 8608 roughness profiles for Classes A, C, and E. (b) Bridge midspan displacement. (c) Vehicle body vertical displacement. (d) Bridge midspan acceleration. (e) Vehicle body vertical acceleration.

Road roughness significantly affects the dynamic component of both bridge and vehicle responses. Under Class A roughness, bridge displacement and vehicle body displacement remain close to the quasi-static deflection under the vehicle weight (Figure 17 b, c). Classes C and E introduce progressively larger dynamic oscillations, particularly in the vehicle body, which is directly excited by the road profile through the suspension: the vehicle body acceleration amplitude under Class E roughness exceeds that of Class A by over an order of magnitude (Figure 17 e). The bridge midspan acceleration (Figure 17 d) shows a comparatively smaller sensitivity to roughness class for this lightweight vehicle, as the bridge dynamics are dominated by its own modal response rather than the roughness-induced contact forces. For heavier vehicles, road rough-

ness would play a larger role in the bridge acceleration, confirming that surface condition is an important excitation source for indirect bridge monitoring applications [3,23].

5.4 Effect of Background Traffic

The preceding analyses considered a single vehicle in isolation. In practice, bridges carry multiple vehicles simultaneously, and the resulting background traffic loads modify the bridge response amplitude. This study investigates whether background traffic affects the relative accuracy of the decoupled approach. The 30 m bridge (Eshkevari configuration) is loaded with both the commercial vehicle and the heavy truck as the instrumented sensing vehicle, while background traffic is modelled as a uniformly distributed random nodal force whose total magnitude corresponds to n vehicles of 2000 kg each, with $n = 0, 5, 10, 20$.

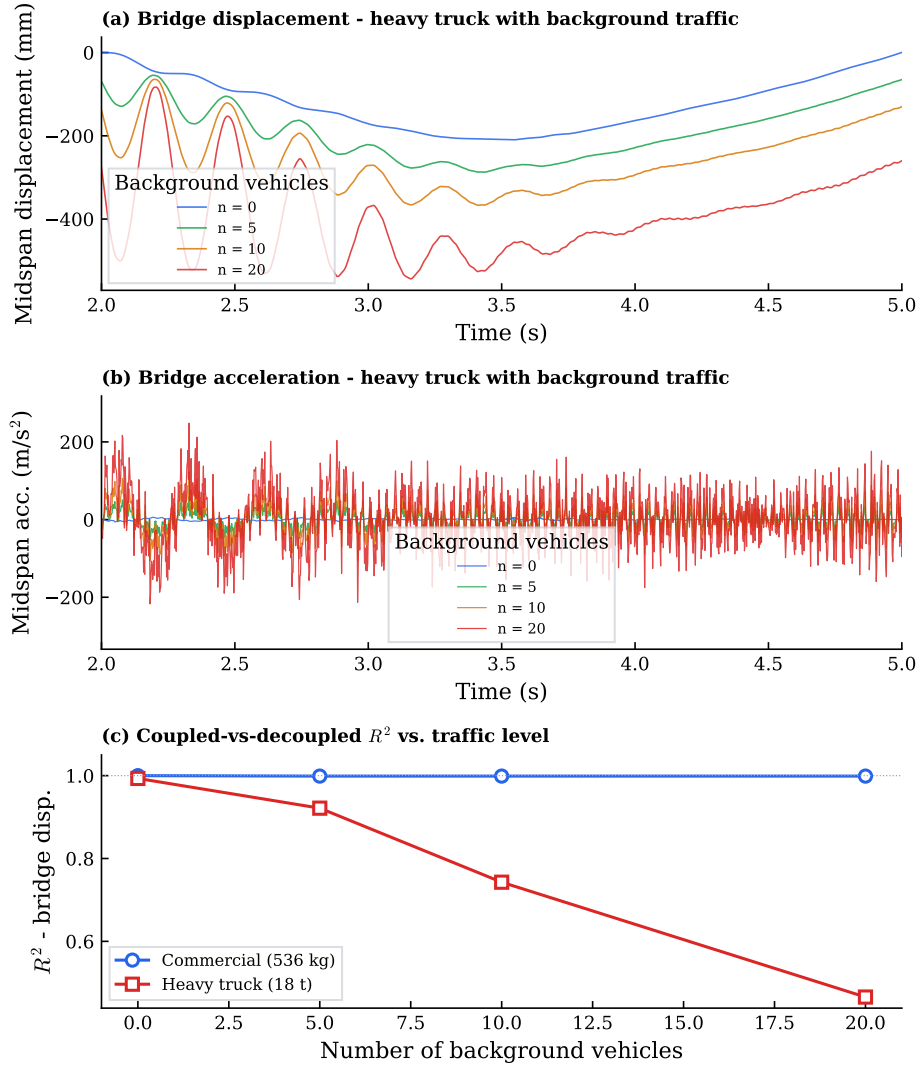


Figure 18: Effect of background traffic on bridge response (30 m bridge, heavy truck, coupled analysis). (a) Bridge midspan displacement with increasing traffic levels. (b) Bridge midspan acceleration with increasing traffic levels. (c) Coefficient of determination R^2 between coupled and decoupled analyses as a function of the number of background vehicles, for both vehicle types.

Background traffic increases both the bridge displacement and acceleration amplitudes substantially (Figure 18 a, b). The coefficient of determination R^2 between coupled and decoupled analyses (Figure 18 c) decreases with the number of background vehicles for both vehicle types, dropping most sharply from the isolated vehicle case ($n = 0$) to moderate traffic ($n = 5$). For the commercial vehicle, R^2 stays close to unity across all traffic levels, while for the heavy truck R^2 continues to decrease, indicating progressively

worse agreement as traffic increases. The deterioration occurs because heavier total loading produces larger bridge deflections, which in turn amplify the dynamic contact forces that the decoupled approach neglects. Nevertheless, the ordering between the two vehicle types is preserved at all traffic levels: the heavy truck consistently produces lower R^2 than the commercial vehicle, reinforcing the mass ratio as the primary determinant of decoupled accuracy.

5.5 Multi-Span Bridge Configuration

The framework supports multi-span continuous bridges by specifying intermediate support locations. This capability is demonstrated using a two-span bridge crossed by a fleet of ten vehicles. The fleet is generated by perturbing a base two-axle composite half-car (comp2) configuration: sprung mass, suspension stiffness, and suspension damping are each independently sampled from a uniform distribution with $\pm 30\%$ range about their base values ($[0.7, 1.3] \times \text{base}$). Entry times are spaced along the approach segment so that vehicles enter the bridge sequentially, and all vehicles travel at the same nominal speed (20 m/s). The same random-fleet procedure is used in the parametric studies that involve background traffic.

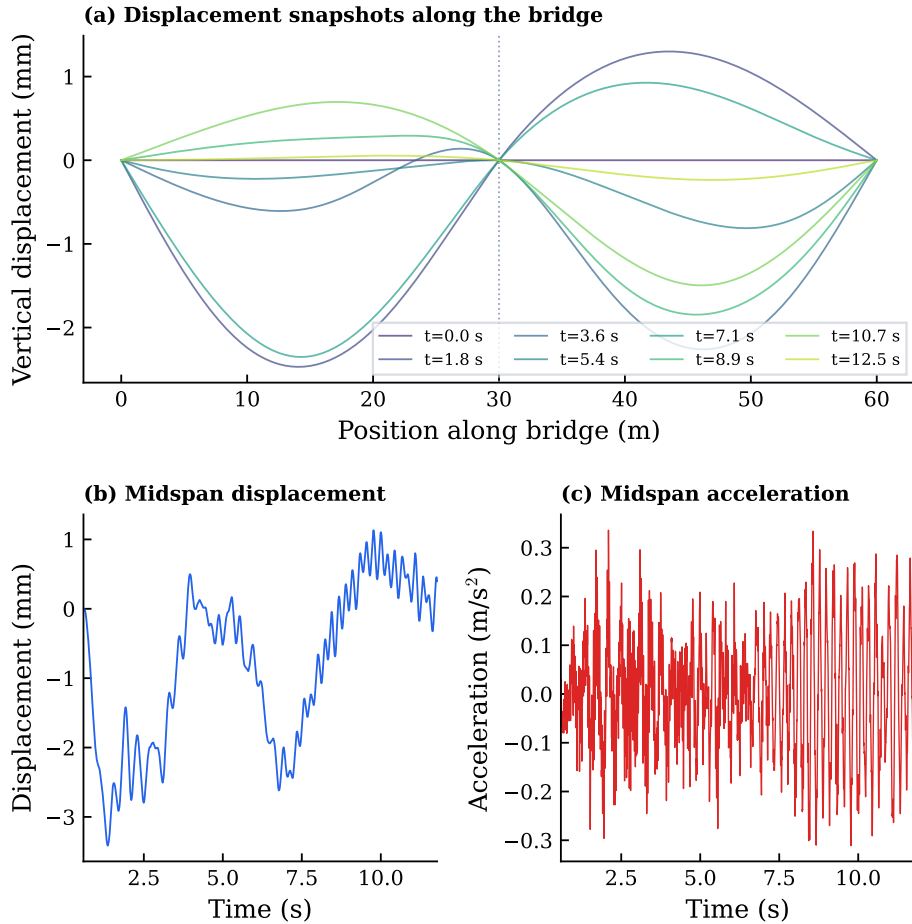


Figure 19: Two-span continuous bridge (2×30 m) under a fleet of 10 randomly generated vehicles: (a) bridge displacement envelope over the full span showing the deflected shape at different time instants; (b) midspan displacement time history of the first span; (c) midspan acceleration time history of the first span.

The two-span bridge analysis demonstrates the framework's capability to handle continuous bridges with multiple vehicles. The displacement snapshots show the characteristic shape of a continuous beam under moving loads, with the inflection point at the intermediate support and alternating deflections in the two spans as vehicles traverse them.

6 Discussion

The validation studies and parametric investigations presented in the previous sections support several key observations about the proposed framework and the VBI problem in general.

The framework’s approach of using OpenSees as a black-box solver for both the bridge and vehicle subsystems offers several practical advantages. First, it enables researchers familiar with OpenSees to perform VBI analyses without learning a new software package or implementing custom finite element formulations. The bridge model can incorporate any element type available in OpenSees, including nonlinear beam-column elements for inelastic bridge response, fibre sections for distributed plasticity, and specialised elements for soil-structure interaction. Similarly, the vehicle model can be extended to include nonlinear suspension behaviour or multi-body kinematics using the full range of OpenSees materials and elements. Second, the rebuild-per-step strategy, while computationally less efficient than maintaining a persistent model, provides robustness: each time step starts from a clean state, eliminating the risk of accumulated numerical errors or state conflicts between the vehicle and bridge models.

The parametric study on the decoupled approach provides quantitative guidance for practitioners. For the lightweight commercial vehicle (536 kg), the coefficient of determination R^2 between coupled and decoupled bridge displacement remains above 0.999 across all four spans tested (15–100 m), confirming that a vehicle of this mass has negligible inertial effect regardless of bridge configuration. For the heavy truck (18,000 kg), the agreement is noticeably weaker and drops furthest on the 15 m bridge where the truck outweighs the bridge by a factor of 24. The mass ratio μ is the dominant predictor of decoupled accuracy: the vehicle body acceleration R^2 follows the same trend as the bridge displacement R^2 but with a larger gap between vehicle classes, reflecting the amplification of interaction effects through the suspension dynamics.

The speed study shows that higher vehicle speeds produce larger dynamic amplification in both bridge and vehicle responses, consistent with the well-known speed parameter effect in moving load problems. The roughness study shows that surface condition substantially affects the vehicle body response (Class E acceleration amplitudes exceed Class A by over an order of magnitude) while the bridge midspan response remains comparatively insensitive to roughness for this lightweight vehicle. The traffic study reveals that background traffic weakens the coupled-vs-decoupled agreement, with the heavy truck R^2 decreasing noticeably as the number of background vehicles grows from 0 to 20, while the commercial vehicle remains close to 1 throughout. The deterioration occurs because the additional loading amplifies bridge deflections and, consequently, the dynamic contact forces neglected by the decoupled approach. Nevertheless, the ordering between vehicle types is preserved at all traffic levels, reinforcing the mass ratio as the primary determinant of decoupled accuracy [9,23].

The open-source nature of the framework addresses a longstanding gap in the VBI research community. While the theoretical foundations are well established, the lack of shared, validated, and documented implementations has led to unnecessary duplication of effort and made it difficult to reproduce published results. By building on the widely used OpenSees platform and providing a complete Python implementation with benchmark configurations, the framework lowers the barrier to entry for researchers and practitioners interested in VBI analysis and indirect bridge monitoring.

6.1 Limitations

The current implementation has several limitations that should be noted. First, the framework is restricted to two-dimensional (planar) analysis, neglecting lateral and torsional dynamics of both the bridge and the vehicle. For straight, single-lane bridges loaded by vehicles travelling along the centreline, this is a reasonable approximation; for curved bridges, multi-lane loading, or vehicles with roll dynamics, a three-dimensional extension would be necessary. Second, the bridge is modelled with Euler-Bernoulli beam theory, which assumes that shear deformation is negligible. For deep beams or short-span bridges, Timoshenko beam elements would provide more accurate results. Third, the tyre-road contact is modelled as a point contact with no loss of contact (though wheel uplift is checked); a more detailed contact model would be needed for rough roads at high speeds. Fourth, the rebuild-per-step strategy incurs computational overhead that could be reduced by maintaining persistent OpenSees models and updating only the time-varying quantities. These limitations represent opportunities for future development.

7 Conclusions

This paper presented an open-source Python framework for vehicle-bridge interaction analysis built on the OpenSees finite element platform. The key contributions are:

1. A modular VBI framework using standard FE software. The framework models the bridge and vehicle as independent OpenSees finite element subsystems coupled through an external iterative algorithm. No custom element formulations or source code modifications to OpenSees are required. This approach makes VBI analysis accessible to the broad community of OpenSees users and allows seamless integration with existing bridge modelling workflows.
2. Support for multiple vehicle model types. Five vehicle models of increasing complexity are implemented, from simple quarter-car spring-mass systems to half-car vehicles with body pitch, axle masses, and independent tyre-suspension assemblies. All models are constructed using standard OpenSees elements and driven by displacement excitation at the contact points.
3. A validated iterative coupling algorithm. The partitioned iterative scheme converges reliably in 1–4 iterations per time step with a tight tolerance of 10^{-12} and reproduces benchmark results from the literature with high fidelity.
4. A quantified simplified approach. Systematic parametric studies across four bridge spans, two vehicle types spanning more than an order of magnitude in mass, six vehicle speeds, three roughness classes, and four traffic levels demonstrate that the vehicle-to-bridge mass ratio μ is the dominant predictor of decoupled accuracy. For the lightweight commercial vehicle ($\mu < 1$), the coupled and decoupled bridge-displacement histories have R^2 above 0.999 across all spans. For heavy vehicles ($\mu > 0.1$), coupled analysis is necessary, with R^2 dropping noticeably below unity and reaching its lowest values when the vehicle mass approaches or exceeds the bridge mass.
5. Open-source release. The complete framework, including all vehicle configurations and benchmark scripts, is released as open-source software to promote reproducible research in vehicle-bridge dynamics and indirect bridge monitoring.

Future work will extend the framework to three-dimensional analysis, incorporate nonlinear material behaviour for both the bridge and vehicle subsystems, and develop interfaces for real-time data assimilation in drive-by bridge health monitoring applications.

Data Availability

The complete source code and benchmark configurations presented in this paper are openly available at <https://github.com/MTalebi/OpenSees-VBI-Simulation>.

References

- [1] Frýba, L. Vibration of solids and structures under moving loads. 1999.
- [2] Yang, YB, Yau, JD, Wu, YS. Vehicle–bridge interaction dynamics: With applications to high-speed railways. 2004. retrieved from <https://doi.org/10.1142/5541>.
- [3] Yang, YB, Lin, CW, Yau, JD. Extracting bridge frequencies from the dynamic response of a passing vehicle. 2004., pp, 471–493. retrieved from [https://doi.org/10.1016/S0022-460X\(03\)00378-X](https://doi.org/10.1016/S0022-460X(03)00378-X).
- [4] Malekjafarian, A, McGetrick, PJ, OBrien, EJ. A review of indirect bridge monitoring using passing vehicles. 2015., p, 286139. retrieved from <https://doi.org/10.1155/2015/286139>.
- [5] Yang, YB, Zhang, B, Wang, T, Xu, H, Wu, Y. Two-axle test vehicle for bridges: Theory and applications. 2019., pp, 51–62. retrieved from <https://doi.org/10.1016/j.ijmecsci.2018.12.043>.
- [6] Green, MF, Cebon, D. Dynamic response of highway bridges to heavy vehicle loads: Theory and experimental validation. 1994., pp, 51–78. retrieved from <https://doi.org/10.1006/jsvi.1994.1046>.
- [7] Zhu, XQ, Law, SS. Dynamic load on continuous multi-lane bridge deck from moving vehicles. 2002., pp, 697–716. retrieved from <https://doi.org/10.1006/jsvi.2001.3996>.
- [8] OBrien, EJ, McGetrick, PJ, Gonzalez, A. A drive-by inspection system via vehicle moving force identification. 2014., pp, 821–848. retrieved from <https://doi.org/10.12989/sss.2014.13.5.821>.
- [9] OBrien, EJ, Keenahan, J. Drive-by damage detection in bridges using the apparent profile. 2015., pp, 813–825. retrieved from <https://doi.org/10.1002/stc.1721>.
- [10] Gonzalez, A, OBrien, EJ, McGetrick, PJ. Identification of damping in a bridge using a moving instrumented vehicle. 2012., pp, 4115–4131. retrieved from <https://doi.org/10.1016/j.jsv.2012.04.019>.
- [11] Malekjafarian, A, OBrien, EJ. On the use of a passing vehicle for the estimation of bridge mode shapes. 2017., pp, 77–91. retrieved from <https://doi.org/10.1016/j.jsv.2017.02.051>.
- [12] Eshkevari, SS, Pakzad, SN, Takac, M, Matarazzo, TJ. Bridge modal identification using acceleration measurements within moving vehicles. 2020., p, 106733. retrieved from <https://doi.org/10.1016/j.ymsp.2020.106733>.

- [13] Mei, Q, Gul, M, Boay, M. Indirect health monitoring of bridges using Mel-frequency cepstral coefficients and principal component analysis. 2019., pp, 523–546. retrieved-from<https://doi.org/10.1016/j.ymsp.2018.10.006>.
- [14] Mei, Q, Gul, M, Shirzad-Ghaheroudkhani, N. Towards smart transportation system: A vehicle scanning method for bridge health monitoring. 2021., pp, 614–630. retrieved-from<https://doi.org/10.1111/mice.12650>.
- [15] McKenna, F. OpenSees: A framework for earthquake engineering simulation. 2011., pp, 58–66. retrieved-from<https://doi.org/10.1109/MCSE.2011.66>.
- [16] Cantero, D, Sarwar, MZ, Malekjafarian, A, Corbally, R, Makki Alamdari, M, Cheema, P, et al. Numerical benchmark for road bridge damage detection from passing vehicles responses applied to four data-driven methods. 2024., p, 190. retrieved-from<https://doi.org/10.1007/s43452-024-01001-9>.
- [17] Yang, YB, Yau, JD. Vehicle–bridge interaction element for dynamic analysis. 1997., pp, 1512–1518. retrieved-from[https://doi.org/10.1061/\(ASCE\)0733-9445\(1997\)123:11\(1512\)](https://doi.org/10.1061/(ASCE)0733-9445(1997)123:11(1512)).
- [18] International Organization for Standardization. ISO 8608:2016 – mechanical vibration – road surface profiles – reporting of measured data. 2016.
- [19] Zhu, M, McKenna, F, Scott, MH. OpenSeesPy: Python library for the OpenSees finite element framework. 2018. retrieved-from<https://openseespydoc.readthedocs.io>.
- [20] Newmark, NM. A method of computation for structural dynamics. 1959., pp, 67–94.
- [21] Chopra, AK. Dynamics of structures: Theory and applications to earthquake engineering. 2017.
- [22] Cantero, D. VBI-2D: Road vehicle–bridge interaction simulation tool for MATLAB. 2024. retrieved-from<https://github.com/DanielCanteroNTNU/VBI-2D>.
- [23] Gonzalez, A, OBrien, EJ, Li, YY, Cashell, K. The use of vehicle acceleration measurements to estimate road roughness. 2008., pp, 483–499. retrieved-from<https://doi.org/10.1080/00423110701485050>.

Appendix: OpenSees Vehicle Model Topology

Table 6 summarises the OpenSees node layout, element connectivity, and boundary conditions for each of the four vehicle model types. In all models, axle nodes (contact points) are fully fixed and excited through imposed displacement and velocity via the `MultipleSupport` pattern. Non-axle nodes carry lumped mass and are free to respond dynamically. Springs and dashpots are modelled using `zeroLength` elements (1D models) or `twoNodeLink` elements (2D models) with `Elastic` uniaxial materials whose stiffness and damping arguments correspond to the spring constant k and the viscous damping coefficient c , respectively.

Table 6: OpenSees node and element connectivity for each vehicle model type. Axle nodes are constrained as fixed supports and driven by imposed motion; non-axle nodes are free. Element notation $i \rightarrow j$ denotes a spring-dashpot connecting nodes i and j .

Model	ndm	Nodes	Mass assignment	Elements	Notes
one_axle_simple	1	1 (axle, fixed), 2 (body)	m_v at node 2	<code>zeroLength</code> 1→2 (k_v, c_v)	2 DOFs
one_axle_comp	1	1 (contact, fixed), 2 (axle), 3 (body)	m_u at 2, m_s at 3	<code>zeroLength</code> 1→2 (k_t, c_t); 2→3 (k_s, c_s)	3 DOFs
two_axle_comp1	1	1,2 (axles, fixed); 3,4 (axle masses); 5,6 (body halves)	m_u at 3,4; m_s at 5,6	Tyre: 1→3, 2→4; Susp: 3→5, 4→6	6 DOFs, independent halves
two_axle_comp2	2	1,2 (axles, fixed); 5,6 (susp. tops); 7,8 (body at axle x); 9 (CG)	m_v, J_v at 9	Susp: 1→5, 2→6 (<code>twoNodeLink</code>); Rigid links: 5→7→9, 6→8→9 (penalty $\sim 10^6 k_s$)	8 DOFs (2 measured: bounce + pitch)
two_axle_comp3	2	1,2 (contacts, fixed); 3,4 (axle masses); 5,6 (susp. tops); 7,8 (body at axle x); 9 (CG)	$m_{u,r}$ at 3, $m_{u,f}$ at 4, m_v, J_v at 9	Tyre: 1→3, 2→4; Susp: 3→5, 4→6; Rigid links: 5→7→9, 6→8→9	10 DOFs (3 measured: 2 axles + bounce + pitch)

For the half-car models with pitch (comp2 and comp3), the rigid-body connection between the CG node (node 9) and the suspension tops (nodes 5, 6) is implemented using intermediate nodes (7, 8) located at the axle x -coordinates but at body height. The `twoNodeLink` elements connecting nodes 7→9 and 9→8 carry penalty stiffness in all three DOFs (x -translation, y -translation, and rotation), ensuring that the body moves as a rigid bar between the two suspension attachment points. The `zeroLength` elements connecting nodes 5→7 and 6→8 similarly enforce kinematic compatibility between the suspension tops and the body endpoints. This penalty-based approach avoids the need for multi-point constraints and is compatible with OpenSees' standard analysis procedures.

Framework Module Pseudocodes

The following pseudocodes summarise the supporting framework modules as step-by-step procedures for readers who prefer the algorithmic form. They restate, in algorithmic notation, the operations described narratively in Sections 3.2, 3.3, 3.4, and 3.7. The main coupled and decoupled procedures appear as Algorithms 1 and 2 in Section 3.

Algorithm 3 Bridge Finite Element Construction and Time Stepping

Require: Span L , support locations, EI , \bar{m} , ζ , discretisation N_e , initial conditions $\{w_n, \dot{w}_n, \ddot{w}_n\}$, nodal forces F , time step Δt

Ensure: Bridge response at t_{n+1} : $\{w_{n+1}, \dot{w}_{n+1}, \ddot{w}_{n+1}\}$

- 1: `ops.wipe()` ▷ Clear previous model
 - 2: Define $N_n = N_e + 1$ nodes at spacing $\Delta x = L/N_e$
 - 3: Apply boundary conditions: pin at first support, roller(s) at remaining
 - 4: Assign lumped mass: $m_j = \bar{m} \Delta x$ (interior nodes), $\bar{m} \Delta x/2$ (end nodes)
 - 5: Define `elasticBeamColumn` elements with A, E, I
 - 6: Eigenvalue analysis: $\omega_1, \omega_2 \leftarrow \text{ops.eigen}(N_{\text{modes}})$
 - 7: Rayleigh damping: $\alpha_M, \beta_K \leftarrow \text{solve } \zeta = \frac{1}{2}(\alpha_M/\omega_i + \beta_K \omega_i)$ for $i = 1, 2$
 - 8: `ops.rayleigh`($\alpha_M, \beta_K, 0, 0$)
 - 9: Apply nodal forces F via `Path` time series and `Plain` load pattern
 - 10: Set initial conditions: `setNodeDisp`, `setNodeVel`, `setNodeAccel` at each node
 - 11: Configure `Newmark` integrator ($\gamma = 0.5, \beta = 0.25$)
 - 12: `ops.analyze`(1, Δt)
 - 13: Extract updated $\{w_{n+1}, \dot{w}_{n+1}, \ddot{w}_{n+1}\}$ via `nodeDisp`, `nodeVel`, `nodeAccel`
-

Algorithm 4 Vehicle Finite Element Construction and Time Stepping

Require: Vehicle properties (masses, stiffnesses, dampings), model type, initial conditions, axle displacements $\{u_i\}$ and velocities $\{\dot{u}_i\}$

Ensure: Vehicle response at t_{n+1} , axle reaction forces $\{F_{a,i}\}$

- 1: `ops.wipe()`
 - 2: if `model` $\in \{\text{one_axle_simple}, \text{one_axle_comp}\}$ then
 - 3: Define 1D model (`ndm`= 1)
 - 4: Create axle contact node(s), fix all DOFs
 - 5: Create body/axle-mass nodes with lumped masses
 - 6: Define `zeroLength` spring-dashpot elements (k, c)
 - 7: else if `model` $\in \{\text{two_axle_comp2}, \text{two_axle_comp3}\}$ then
 - 8: Define 2D model (`ndm`= 2, `ndf`= 3)
 - 9: Create axle contact nodes, fix all DOFs
 - 10: Create CG node with body mass m_v and rotational inertia J_v
 - 11: Create intermediate nodes at axle x -coordinates
 - 12: Define `twoNodeLink` suspension elements
 - 13: Define penalty links ($k_{\text{pen}} \approx 10^6 k_s$) for rigid-body connection
 - 14: end if
 - 15: Apply `MultipleSupport` with `imposedMotion` at each axle node
 - 16: Prescribe displacement $u_i(t)$ and velocity $\dot{u}_i(t)$ via `Path` time series
 - 17: Set initial conditions from previous time step
 - 18: Configure `Newmark` integrator ($\gamma = 0.5, \beta = 0.25$)
 - 19: `ops.analyze`(1, Δt)
 - 20: `ops.reactions`(-dynamic, -rayleigh)
 - 21: $F_{a,i} \leftarrow \text{nodeReaction}(i)$ for each axle node
-

Algorithm 5 ISO 8608 Road Roughness Profile Generation

Require: Roughness class coefficient $G_d(n_0)$, spatial range $[x_0, x_{\max}]$, mesh size Δx , bridge span L

Ensure: Roughness profile $r(x_j)$

- 1: $\Delta n \leftarrow \min(0.01, 1/(2L))$ ▷ Avoid periodicity within bridge span
 - 2: $n_l \leftarrow \min(0.01, \Delta n)$, $n_u \leftarrow 10$ cycles/m
 - 3: Generate spatial frequency array: $n_k = n_l, n_l + \Delta n, \dots, n_u$
 - 4: Compute PSD: $G_d(n_k) = G_d(n_0) \cdot (n_k/n_0)^{-2}$, $n_0 = 0.1$ cycles/m
 - 5: Compute amplitudes: $A_k = \sqrt{2 G_d(n_k) \Delta n}$
 - 6: Generate random phases: $\phi_k \sim \mathcal{U}[0, 2\pi]$
 - 7: Generate position array: $x_j = x_0, x_0 + \Delta x, \dots, x_{\max}$
 - 8: for each position x_j do
 - 9: $r(x_j) = \sum_k A_k \cos(2\pi n_k x_j + \phi_k)$
 - 10: end for
 - 11: Optional: Apply moving-average smoothing (window size w)
-

Algorithm 6 Vehicle-to-Bridge Force Mapping

Require: Axle positions $\{x_{a,i}\}$, dynamic reaction forces $\{F_{a,i}\}$, static axle weights $\{W_i\}$, bridge node coordinates, bridge span L

Ensure: Equivalent nodal force vector F_{inter}

- 1: Initialise $F_{\text{inter}} \leftarrow 0$
 - 2: for each axle i do
 - 3: $F_{\text{total},i} \leftarrow W_i + F_{a,i}$ ▷ Static weight + dynamic reaction
 - 4: if $x_{a,i} < 0$ or $x_{a,i} > L$ then ▷ Axle off bridge
 - 5: continue
 - 6: end if
 - 7: if $F_{\text{total},i} > 0$ then ▷ Wheel uplift detected
 - 8: Set $F_{\text{total},i} \leftarrow 0$ and flag warning
 - 9: end if
 - 10: Find element $[x_j, x_{j+1}]$ containing $x_{a,i}$
 - 11: $\xi \leftarrow (x_{a,i} - x_j)/(x_{j+1} - x_j)$ ▷ Local coordinate
 - 12: $F_j \leftarrow F_j + (1 - \xi) F_{\text{total},i}$
 - 13: $F_{j+1} \leftarrow F_{j+1} + \xi F_{\text{total},i}$
 - 14: end for
-